This manuscript has been submitted for publication in *JGR: Solid Earth*
Please note that this article has not been peer-reviewed and is currently undergoing peer review for the first time. Subsequent versions of this manuscript may have slightly different content.

3D dynamic rupture modeling of the 2021 Haiti earthquake used to constrain stress conditions and fault system complexity

H. Zoe Yin[1], Mathilde Marchandon[2], Jennifer S. Haase[1], Alice-Agnes Gabriel[1,2], Roby Douilly [3]

[1]Scripps Institution of Oceanography, UCSD, La Jolla, CA, USA
[2]Department of Earth and Environmental Sciences, Ludwig Maximilian University of Munich, Munich, Germany
[3]University of California, Riverside, CA, USA

Key Points:

- Dynamic rupture modeling shows that regional stress shape, orientation, and geometric complexity are key controls on the 2021 Haiti rupture.
- Regional stress shape and orientation may be highly variable within the southern peninsula of Haiti.
- Geometric complexity plays a large role in ongoing rupture segmentation of Haiti's southern peninsula.

Corresponding author: Jennifer S. Haase, jhaase@ucsd.edu

Abstract

The 2021 M_w7.2 Haiti earthquake was a devastating event which occurred within the Enriquillo Plantain Garden Fault Zone (EPGFZ). It is not well-understood why neither the 2021 nor the prior M_w7.0 2010 earthquake were simple strike slip events and, instead, ruptured with distinct patches of dip slip and strike slip motion on largely separate fault planes. We develop several 3D dynamic rupture simulations of the 2021 earthquake to test which conditions may have controlled the complex rupture. The major characteristics of the earthquake rupture include: the characteristic spatial and temporal separation of strike-slip and dip-slip motion, rupture transfer to the Ravine du Sud Fault (RSF), and a multi-peak source time function. We construct a detailed fault system geometry which includes a north-dipping Thrust Fault (TF) and near-vertical RSF, along with surrounding regional and secondary faults. We find that along-strike changes to the frictional strength of the TF are needed to focus the slip to reproduce the scale and pattern of deformation observed with InSAR. Lateral changes in the regional stress shape and orientation are key to reproducing the observed rupture transfer from the TF to the RSF while maintaining the rake required to reproduce the broad InSAR surface deformation pattern and multi-peak source time function. The dynamic rupture modeling results suggest that significant variability in fault stress and strength as well as complexities of the subsurface geometry may have been key controls on the dynamics of the 2021 rupture.

Plain Language Summary

The southern peninsula of Haiti experiences high seismic hazard and has endured catastrophic impacts from past major earthquakes, most notably the 2010 M_w7.0 earthquake which was one of the deadliest earthquakes on record globally. In 2021, a M_w7.2 earthquake killed over 2000 people and underlined the importance of better understanding the hazardous Enriquillo Plantain Garden Fault Zone (EPGFZ) which produced both of these destructive events. Both events were considerably more complex than was previously thought to be typical based on the geologic record and raise interesting questions about what conditions drive earthquake ruptures in this region. In this study, we develop numerical models (i.e. dynamic rupture models) of the 2021 earthquake which explore which conditions may have driven the observed rupture characteristics. We find that the the accumulation of stress on the fault planes likely has large variability and, along with fault geometry and strength complexity, may have contributed to the observed 2021 rupture. These findings have implications for characterizing seismic hazard in this region.

1 Introduction

The 2021 M_w7.2 Haiti earthquake led to more than 2200 deaths and struck just over a decade after the devastating 2010 M_w7.0 earthquake which was one of the deadliest earthquakes recorded globally. Both events occurred within a complex network of faults comprising the Enriquillo Plantain Garden Fault Zone (EPGFZ), which spans the Tiburon Peninsula in southern Haiti (Figure 1). Although the main Enriquillo Plantain Garden Fault (EPGF) has historically been mapped as a near-vertical fault which accommodates purely strike slip motion, neither the 2010 nor the 2021 event had a simple strike-slip focal mechanism, nor did either clearly rupture this well-known fault as it is mapped. Instead, both recent ruptures initiated on a north-dipping fault segment which hosted significant dip slip motion and then transferred westward to an adjacent steeply-dipping fault segment with primarily strike slip motion (Calais et al., 2022; Li & Wang, 2023; Okuwaki & Fan, 2022; Wen et al., 2023; Yin et al., 2022). Both events also had major slip occurring off of the mapped EPGF fault: the 2010 event ruptured the blind Léogane thrust fault with seemingly no major slip accommodated on the EPGF, while the 2021 earthquake has been proposed to have initiated on a north-dipping thrust

fault (it is unclear whether this is the EPGF or an unmapped fault) and then transferred westward to the mapped Ravine du Sud fault (Douilly et al., 2023; Raimbault et al., 2023) (Fig. 1). Major questions remain about the fault geometry responsible for the 2021 event and how that geometry relates to the known fault system. It is also still not well understood why neither the 2010 nor 2021 event was a simple strike slip event and, instead, each ruptured with two distinct patches of dip slip and strike slip motion on largely separate fault planes.

The combination of dip slip and strike slip motion observed in both 2010 and 2021 earthquakes is not unexpected given the tectonic setting of this fault zone. The EPGFZ occurs within the boundary between the North American (NA) and Caribbean (CAR) plates, which collide obliquely at an estimated rate of 18–20 mm/yr (DeMets et al., 2000). The Septentrional Fault, North Hispaniola fault, and the EPGFZ together accommodate both left-lateral and shortening motion, with the EPGFZ accommodating roughly half of the NA-CAR relative motion. A network of GNSS (Global Navigation Satellite System) stations throughout the region has allowed for the mapping of strain accumulation across the plate boundary (Calais et al., 2023; S. Symithe et al., 2015). Block modeling using GNSS data suggests two competing models for strain accumulation: The first model proposes that the EPGFZ accommodates about 6–7 mm/yr of left-lateral strike-slip motion, while the Jeremie-Malpasse (JM) reverse fault system off of the north shore of the Southern Peninsula (Fig. 1) is responsible for accommodating 6–7 mm/yr of north-south shortening (plate boundary-perpendicular motion). The second model proposes that the transpressive motion is accommodated primarily by the EPGFZ, with offshore thrust faults playing a less important role in shortening (Calais et al., 2023). A better understanding of where transpression is localizing and driving seismicity is needed to improve understanding of seismic hazard.

The 2010 earthquake rupture occurred to the east of the 2021 rupture (Fig. 1) and both events increased Coulomb Failure Stress (CFS) on the section of the EPGF between the two ruptures (Calais et al., 2022; S. J. Symithe et al., 2013). This segment of the EPGF, however, has remained unruptured by either earthquake, raising the question of whether it is locked and seismically loaded or if it is accumulating or accommodating strain in some other way. Interestingly, centimeter-scale shallow creep was observed on sections of this unruptured segment following both the 2010 and 2021 events (Maurer et al., 2022; Yin et al., 2022).

Seismic and geodetic observations surrounding the 2021 earthquake provide critical insights into the dynamic rupture process. The event was recorded by the Ayïti-Seismes network, which, at the time of the earthquake, included four accelerometers (three of which were Raspberry Shake stations hosted by residents), and three broadband seismometers (Calais et al., 2022). Data from these stations were used to precisely locate a large cluster of aftershocks in the eastern portion of the rupture broadly delineating a north-dipping structure, with a more sparse cluster of aftershocks to the west indicating a near-vertical structure approximately coincident with the mapped RSF (Douilly et al., 2023). Interferometric Synthetic Aperture Radar (InSAR) geodetic imagery was captured from ALOS-2 and Sentinel-1 satellite missions, which resolved a detailed spatial pattern of co- and post-seismic ground deformation. Unwrapped InSAR interferograms showed deformation in the direction of the Line-of-Sight (LOS) of the observing satellite. Ascending and descending InSAR observations of the 2021 event constrained a region of uplift in the eastern part of the rupture consistent with thrust motion on a north-dipping structure, while fault-parallel motion dominated to the west, concentrating on the Ravine du Sud fault where the InSAR captured rupture reaching the surface (Li & Wang, 2023; Raimbault et al., 2023; Yin et al., 2022). GNSS offsets, which provide absolute static deformation measurements across the peninsula, confirmed the broad pattern of deformation observed in the InSAR data (Raimbault et al., 2023). Saint Fleur et al. (2024) conducted fieldwork following the 2021 event focused on documenting extensive surface cracking

in response to the coseismic rupture. In the west, strike-slip cracks dominated, while the eastern section exhibited primarily thrust faulting. This variation aligns with the earthquake's mixed-mode rupture mechanism.

Several studies have investigated the slip distribution and fault geometry of the 2021 M_w 7.2 Haiti earthquake (i.e., Calais et al., 2022; Goldberg et al., 2022; Li & Wang, 2023; Maurer et al., 2022; Okuwaki & Fan, 2022; Raimbault et al., 2023; Wen et al., 2023). Despite differences in the inversion methods, considered observation datasets, and fault geometry, most inversion studies agree on the earthquake breaking at least two main fault segments. The rupture nucleated on an eastward north-dipping thrust segment where the slip reached ∼2.5-3 m without rupturing the surface. Then the rupture transferred westward to a sub-vertical strike-slip segment (broadly agreed to be the RSF) with ∼1-2 m of slip reaching the surface. Interestingly, the rupture does not clearly align with the previously mapped vertical EPGF. Kinematic models consistently inferred source time functions (STFs) that contain at least two main peaks at 5-8 sec and 15-20 sec after the origin time, likely each coincident with a corresponding segment. STFs are in agreement with back-projection results that show two strong seismic radiation episodes with roughly the same timing.

Despite the extensive work that's been done to understand the tectonics in Haiti through data collection networks (e.g. Calais et al., 2022; Raimbault et al., 2023; S. Symithe et al., 2015), geophysical surveys (e.g. Calais et al., 2023), and geologic mapping (e.g. Mercier de Lépinay et al., 2011; Prentice et al., 2010; Prentice et al., 2003; Saint Fleur et al., 2015, 2020, 2024), gaps remain in our understanding of the complex faulting that drives seismic hazard, including the 2021 event.

Significant advances in the capabilities of dynamic rupture modeling techniques, enabled in part by the proliferation of high performance computing, provide an opportunity to understand the complex dynamics of the 2021 earthquake through 3D dynamic rupture simulation. Unlike kinematic or static slip inversions, which solve for slip distributions that sufficiently satisfy detailed observations, dynamic rupture models are forward simulations with a prescribed set of initial conditions and model parameters that allow the rupture to unfold spontaneously. Initial conditions consider fault geometry, material properties, fault strength (e.g., frictional properties, critical distance), and a description of pre-event stress on the fault. With these initial conditions it is possible to solve for the dynamic evolution of the rupture including fully dynamic wave propagation and permanent deformation (Harris et al., 2011; Harris et al., 2018; Ramos et al., 2022). While kinematic models can illuminate when and where slip occurred, dynamic rupture models can probe why the fault ruptured in a particular way, providing unique insights into the conditions that drove rupture. Dynamic rupture simulations have been used to study fundamental aspects of earthquake physics (e.g. Douilly et al., 2015; Gabriel et al., 2023), to assess earthquake hazards (e.g. Aochi & Ulrich, 2015; Douilly et al., 2017), to recreate notable rupture patterns in past earthquakes (Ma et al., 2008; Wollherr et al., 2019) and to discriminate between competing models of fault system geometries and faulting mechanisms (e.g. Palgunadi et al., 2020; Ulrich et al., 2019). In this study, we focus on identifying the conditions that control key observations of the 2021 M_w7.2 Haiti earthquake. Using the dynamic rupture models, we simulate InSAR surface deformations, GNSS offsets, and source time functions to compare with observations. We aim to understand key rupture characteristics that are inferred from the observations, primarily the spatial and temporal separation of left-lateral and reverse fault slip, and rupture transfer from the initial fault to the RSF to better understand the conditions that lead the observed rupture.

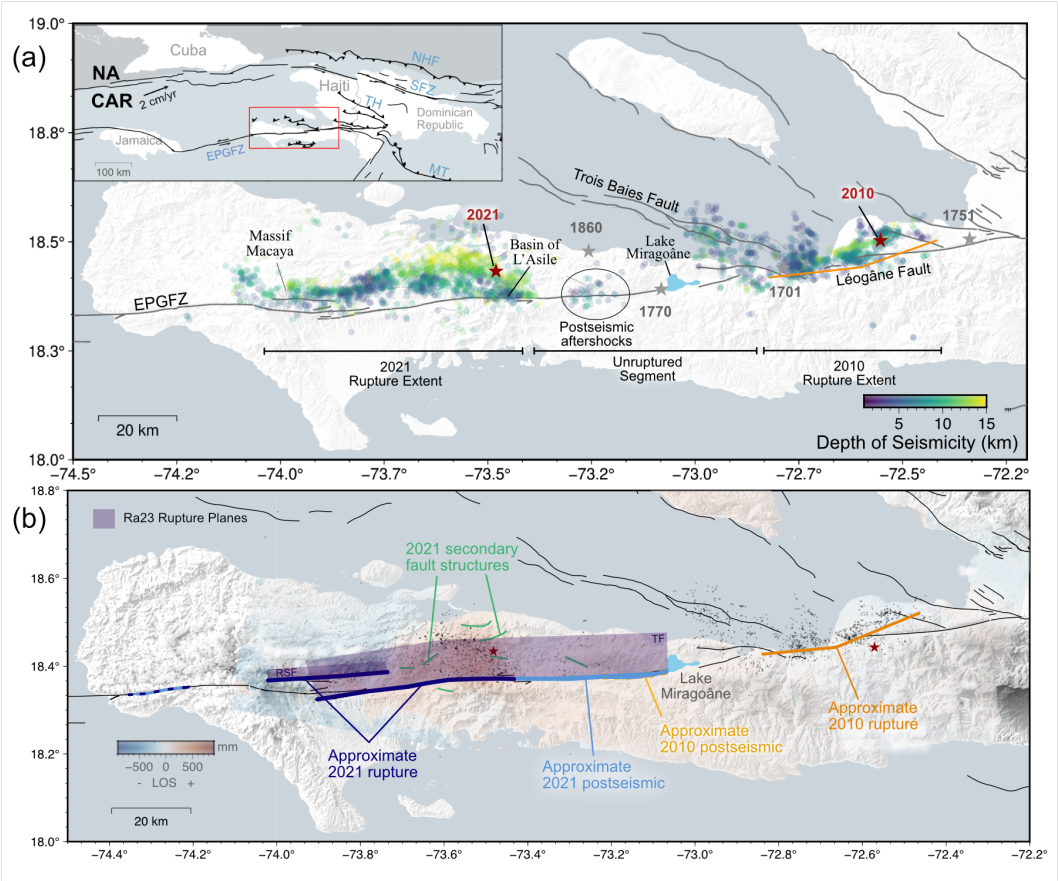

Figure 1: Overview of the tectonic setting of the 2021 earthquake. Top left inset shows the North American (NA) and Caribbean (CAR) tectonic plates. (a) Overview of the southern peninsula of Haiti, highlighting major geographic markers, 2010 and 2021 rupture extents and aftershocks, and historic earthquakes. Major historic earthquakes are marked by stars, with red stars highlighting the locations of the 2021 M_w7.2 and 2010 M_w7.0 epicenters; Aftershock locations are shown with circles, colored by event depths. Aftershock locations following the 2010 event are from Douilly et al. (2013), aftershock locations following the 2021 event are from Douilly et al. (2023). (b) Descending InSAR unwrapped interferogram is overlaid on topography, where red indicates the region of surface uplift over the eastern part of the rupture north of the fault. The two main fault planes used in this study, the Thrust Fault (TF), and the Ravine du Sud Fault (RSF) are shown with purple transparent rectangles. The approximate extent of rupture is taken from InSAR data.

2 Methods and Model Setup

We solve the coupled dynamic rupture and seismic wave propagation problem using the open-source software SeisSol (`https://github.com/SeisSol/`). SeisSol is optimized for high performance computing, utilizing a Discontinuous Galerkin discretization with arbitrary high-order derivative (ADER) time integration and local time stepping on unstructured adaptive tetrahedral meshes (Dumbser & Käser, 2006; Heinecke et al., 2014; Krenz et al., 2021; Uphoff et al., 2017). SeisSol allows for the combination of geometrically complex fault structures with region-specific fault and material properties. This is critical in Haiti where the geometric complexity of the fault zone has been

interpreted to be central to the mechanics and strain partitioning of the EPGF fault system (Douilly et al., 2013; S. J. Symithe et al., 2013; Wang et al., 2018).

To construct a 3D dynamic rupture model, we must prescribe a set of parameters and initial conditions which govern the rupture including fault geometry, material properties, relative fault strength, and initial stress orientation and magnitude (Ramos et al., 2022). We choose parameters that reflect the best-available data and regional knowledge. In cases where relevant properties are unknown, we conduct sensitivity tests to determine the range of parameter values that allow for the reproduction of the earthquake observable. These parameters and initial conditions are described below.

2.1 Fault System Geometry

Fault geometry is a primary control on rupture evolution (Nielsen et al., 2000). We develop a highly complex fault mesh to reproduce the Haiti rupture, with 17 non-planar, 3D fault segments that curve and intersect over a 200+ km domain to accurately capture the fault complexity documented in the region. This geometry combines results from several sources including mapped faults and slip inversion studies (Fig. 2). The geometry of the main two faults involved in the 2021 rupture is adapted from the Raimbault et al. (2023) study which distributes cosesismic slip from the 2021 event on two faults: (1) a thrust fault running subparallel to the EPGF (possibly the EPGF itself or a separate structure), herein called the Thrust Fault (TF) which dips north 66 $\pm$ 4°; and (2) the Ravine du Sud Fault (RSF) which is a mapped near-vertical fault, dipping north 86 $\pm$ 2° (Fig. 2). We extend the TF eastward from 73.2°W (where the Raimbault et al. geometry ends, Fig. 1) to Lake Miragoane, following the mapped EPGF trace to allow for the possibility that this is a continuous structure. Raimbault et al. (2023) developed this fault geometry based on a nonlinear kinematic finite fault slip inversion constrained by teleseismic data in Calais et al. (2022). Centimeter-scale offsets across linear features located 10-20 km away from the main fault were observed to slip in the 2 weeks following the earthquake with InSAR imagery (Yin et al., 2022). These features are included to investigate how they behave during the dynamic rupture process and, in the absence of information about fault dip, are assumed to be vertical. We also include the 2010 earthquake rupture geometry which is taken from Douilly et al. (2015). Offshore thrust faults which produced significant aftershock activity following the 2010 earthquake are taken from analysis of seismic reflection surveys in Calais et al. (2023). Finally, surrounding mapped faults are taken from the comprehensive database in Saint Fleur et al. (2020) and are assumed to be vertical.

The computational mesh developed is a box of $700 \times 500 \times 150\text{km}^3$ in the east, north, and vertical direction, respectively. The size is chosen to be large enough to avoid any spurious reflected waves from the non-perfect absorbing boundaries. The top surface of the domain includes the topography from the SRTM global DEM (Farr et al., 2007) downsampled at 1 km. The domain is discretized with tetrahedral elements of variable size using the software *PUMGen* (`https://github.com/SeisSol/PUMGen/`). The mesh resolution is set to an element edge length of 200 m on the fault surfaces and gradually coarsens away from the faults to a maximum edge length of 15 km in the volume. The mesh includes a $300 \times 100 \times 40$ km^3 high-resolution box within which frequencies of at least up to 1 Hz can be resolved. The constructed unstructured tetrahedral mesh consists of 12 million elements. A simulation with 4th-order accuracy in time and space for 30 s requires $\sim$ 1100 CPU hours on the supercomputer SuperMUC-NG at the Leibniz supercomputing center in Garching, Germany.(Douilly et al., 2023) determined from aftershocks of the 2021 earthquake (Table S1). We force nucleation over a radius r_{crit} using friction reduction (see supplemental information).

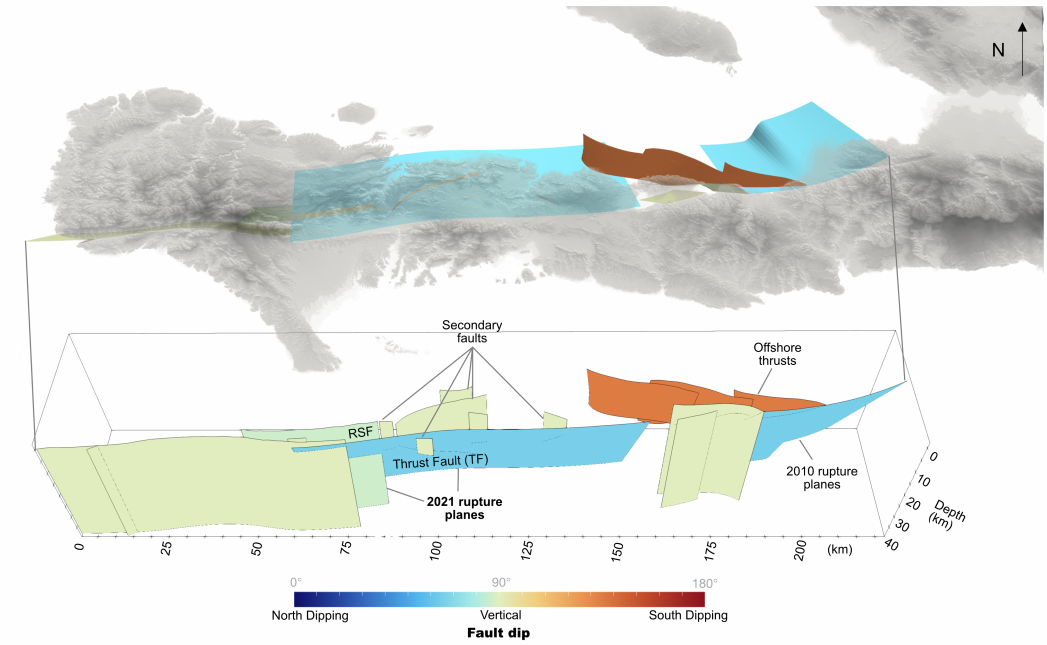

Figure 2: An oblique view of the fault geometry, with the top panel showing a top-down view of the topography of Haiti overlaid on the fault surfaces. The bottom panel shows a slightly adjusted view of the fault surfaces, labeled by source. Faults are colored by fault dip, with green indicating near-vertical faults, blue indicating north-dipping faults, and orange indicating south-dipping faults. 2021 M_w7.2 coseismic rupture planes are taken from Raimbault et al. (2023), secondary faults observed from InSAR data are taken from Yin et al. (2022), offshore thrust faults are modified from Calais et al. (2023), the 2010 M_w7.0 planes are adapted from Douilly et al. (2015), and surrounding mapped faults are taken from Saint Fleur et al. (2020).

2.2 Friction and Fault Strength

A linear slip-weakening (LSW) friction law is used to describe the frictional fault strength (Andrews, 1976; Ida, 1972). Coseismically, the slip-dependent fault weakening behavior governed by aging law rate-and-state friction is similar to that governed by linear slip-weakening friction (e.g., Bizzarri & Cocco, 2003; Garagash, 2021; Kaneko et al., 2008). Fault strength, τ, at any location on the fault is calculated using:

$$\tau = -C - min(0, \sigma_n)(\mu_s - \frac{\mu_s - \mu_d}{D_c} min(S, D_c))$$

Where C is the on-fault frictional cohesion , σ_n is the normal stress, μ_s and μ_d are the static and dynamic coefficients of friction, respectively, D_c is the critical slip distance, and S is the accumulated fault slip. SeisSol convention is that compressive stresses are negative. Faults begin to slip when local shear stress exceeds the local fault strength. Fault strength then decreases linearly from static to dynamic levels over the critical slip distance, D_c, where larger critical distance implies larger fracture energy. μ_s, μ_d, and D_c are defined throughout the fault geometry and are assumed to be spatially uniform, except in some notable circumstances where we vary the value of μ_s on some sections of the TF, as described in the results section. We set on-fault frictional cohesion to 0.5 MPa below 6km on each fault and increase it linearly to 3 MPa at the surface to create a barrier to large surface ruptures.

2.3 Pre-stress Ratio

In a dynamic rupture simulation, only a small part of the fault needs to reach failure in order to initiate sustained rupture. The change in stress at the rupture front and dynamic stresses from seismic waves can raise the local shear stresses to exceed local fault strength, thereby sustaining the rupture. R, or the relative pre-stress ratio (Aochi, 2003; Ulrich et al., 2019), is the ratio of potential stress drop to full breakdown strength drop. The value of R is calculated from three components : 1) initial (static) fault strength, $\tau_y = \sigma_n \mu_s$; 2) final (dynamic) fault strength, $\tau_f = \sigma_n \mu_d$ and 3) initial shear stress, τ_0, resolved on the fault surfaces (Fig. 3).

The potential stress drop can be defined as the difference between initial shear stress and final shear stress ($\tau_0 - \tau_f$), while the potential strength drop is defined as the difference between the initial fault strength and the final shear stress. Under LSW, the final shear stress does not account for rapid co-seismic weakening and restrengthening (Gabriel et al., 2023; Madariaga, 1976) and so is equivalent to the dynamic shear strength. Accordingly, we can define:

$$R = \frac{\tau_0 - \tau_f}{\tau_y - \tau_f}$$

where τ_0 is the initial traction on the fault, τ_f is the final traction on the fault, τ_y is the fault strength which must be exceeded to initiate slip (Fig. 3). We can then define R as:

$$R = \frac{\tau_0 - \mu_d \sigma_n}{(\mu_s - \mu_d)\sigma_n}$$

(Tinti et al., 2021). Fig. 3B shows a schematic profile of the fault stress and strength as a function of depth taken at one location on the fault. In the case of a fault near failure, the initial fault stress (black) will lie between the fault strength (green) and final stress levels (red). If rupture reaches this location on the fault, shear stresses may be brought above the shear strength and then drop to the final shear stress. If at any point the stresses are insufficient to reach the static strength then rupture will not propagate. The values of R can be resolved on any fault surface and depend on the initial stress, fault strength, and final stress on the given fault surface (Fig 4).

The parameter R_0 is used in the implementation of regional stresses, and defines the maximum value of R for a given regional stress tensor (Aochi, 2003). This acts to scale the overall values of R resolved on the fault surfaces.

2.4 Initial Stress State

Following the work of Jia et al. (2023) and Hayek et al. (2024), we consider two main contributions to the stress distribution on the fault surfaces prior to the 2021 event: 1) regional stresses due to the accumulation of long-term regional tectonic loading; and 2) an *a priori* unknown distribution of on-fault stress variations on the fault surfaces which could be driven by the presence of subsurface asperities impacting the accumulation of stress on the fault or remaining stress heterogeneities left from past earthquakes (Fig. 5). We develop dynamic rupture models which consider these sources of stress both separately and in combination to better understand their unique contributions to the observed rupture. We expect the regional stress field to broadly encourage left lateral strike slip and thrust motion on the main two faults, while the heterogeneous stress field may provide a more nuanced spatial pattern of stress concentrations. We note that this setup does not explicitly account for any stresses imparted by the 2010 earthquake. Here we describe the theory and methods used for each of these stress sources.

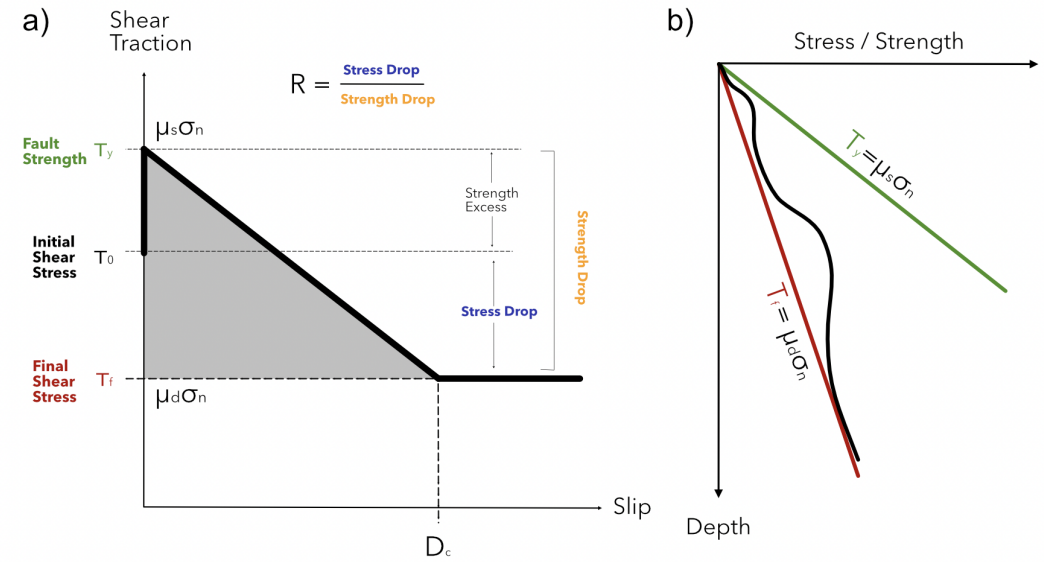

Figure 3: A schematic illustration of the relationship between shear traction, shear stress, and shear strength using Linear Slip Weakening laws; a) Shear traction as a function of slip at a single point on the fault. τ_0 is initial stress, τ_y, is fault strength τ_f is the dynamic shear strength, i.e. the final shear stress of the fault. The strength excess is the difference between τ_y and τ_0 that must be overcome for the fault to fail and initiate slip. D_c is the critical distance over which the fault decreases linearly from static to dynamic fault strength b) A schematic profile of shear stress and strength taken as a function of depth taken as a cross-section on some point on the fault at a single point in time. The black line shows a profile of shear stress with depth, τ_y (green) shows a profile of shear strength with depth, τ_f (red) shows a profile of dynamic strength with depth. Figure adapted from Tinti et al. (2021).

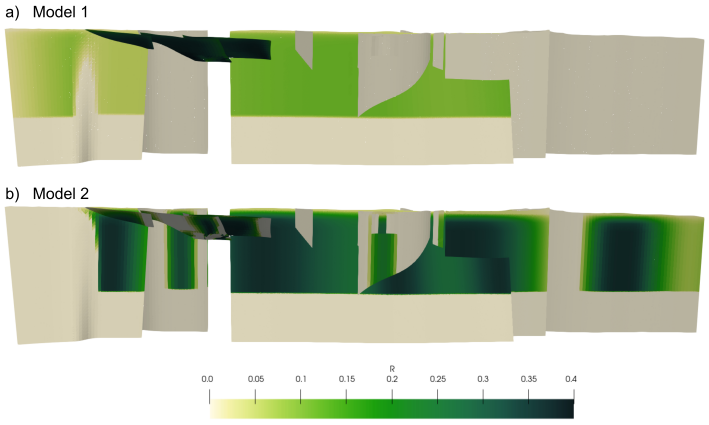

Figure 4: Pre-stress ratio values, R, resolved on the fault surfaces: a) R in the thrust faulting regime where the regional stress tensor has orientation $SH_{max} = 40°$ stress shape ratio, ν=0.5; b) R in the strike-slip faulting regime where the regional stress tensor has orientation $SH_{max} = 50°$ stress shape ratio, ν=0.0;

2.4.1 Regional Stress Field

We calculate a tectonically-driven regional stress state across the Peninsula (Fig. 5), assuming Andersonian stress conditions, where one principal stress component is assumed to be vertical (Heidbach et al., 2018; Simpson, 1997). We define the regional stress field by orienting SH_{max}, the azimuth of the maximum horizontal compressive stress (measured clockwise from north) and defining ν, the stress shape ratio which scales the relative amplitudes of principal stresses.

The stress shape ratio, ν, is defined as:

$$\nu = \frac{s_2 - s_3}{s_1 - s_3}$$

where s_1, s_2, and s_3, are the principal stress components ordered from largest to smallest. The faulting regime impacts the meaning of ν. For example, in a strike-slip faulting regime, ν=0.5 indicates pure strike-slip, $\nu < 0.5$ indicates tanspression, while $\nu > 0.5$ indicates transtension. The faulting regime depends on which component corresponds the maximum horizontal principal stress SH_{max}, the minimum horizontal principal stress, SH_{min}, and the vertical principal stress component, S_v. In the thrust faulting regime, $SH_{max} > SH_{min} > S_v$, whereas in the strike slip faulting regime, $SH_{max} > S_v > SH_{min}$ (Heidbach et al., 2018) (Figure 6).

We calculate the stress tensor at every point on the faults, comprising what we call the "regional-only" stress field (Fig. 5A). We use a stress modulation function, $\Omega(z)$ (Ulrich et al., 2019), to smoothly taper deviatoric stresses to zero at seismogenic depths between 25-28 km, to mimic the brittle ductile transition at the bottom of the seismogenic zone. This depth range is chosen based on the distribution of relocated aftershock seismicity, which is limited, on average, to a depth of 25-30 km (Douilly et al., 2013). Kinematic slip inversions also found the slip distribution to be limited to above 20 km (Calais et al., 2022; Goldberg et al., 2022).

We compare different effective normal stress assumptions (Madden et al., 2022): one where effective normal stress increases with depth throughout the crust with lithostatic stress. Alternatively, we use a fluid over-pressure assumption (Madden et al., 2022; Rice, 1992) in which, at depth, the pore fluid pressure gradient mirrors the lithostatic stress gradient, leading to constant effective normal stress at depth. In our implementation of this assumption, we use a pore fluid pressure ratio of $\gamma = \gamma_{water}/\rho = 0.34$ and taper stresses to 52 MPa at 6 km depth (Gabriel et al., 2023). With lithostatic stress conditions, normal stresses continuously increased with depth, causing large normal stresses on the fault at depth which prevented sustained rupture. When rupture did occur, stress drops tended to be extremely large, producing large slip magnitude (>10 m in some cases), supershear rupture and other unobserved effects. When using the over-pressure condition, we observed more realistic stress drops, slip magnitudes, and rupture velocities. We therefore use this fluid over-pressure assumption in all the following simulations.

2.4.2 Stress heterogeneity on the fault surface

In addition to regional stresses, we additionally consider the presence of heterogeneities in the initial stresses on the fault. We use a Kinematically Informed Heterogeneous Stress technique in which a slip model, in this case taken from a static finite fault slip inversion, is assumed to be the result of some heterogeneous stress distribution on the fault plane prior to the earthquake. In order to quantify this heterogeneous pre-event stress distribution, we run a pseudo-static simulation (Glehman et al., 2024; Tinti, Fukuyama, et al., 2005; Yang et al., 2019) using the same computational mesh and the same fault geometry as the subsequent dynamic rupture simulations. The slip distribution is combined with a time dependent slip rate function to impose an interface condition on all faults that slipped and kinematically compute the stress-change time series to find the

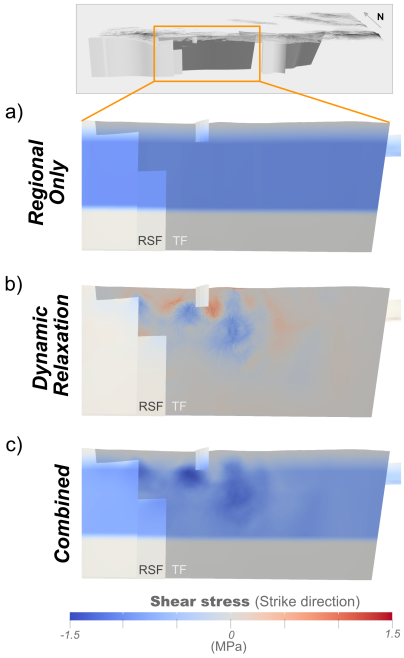

Figure 5: Initial shear stresses resolved on the fault surfaces, where negative shear stresses in the strike direction encourage left-lateral slip. : a) tectonically-driven regional stresses, where deviatoric stresses are tapered to zero below the seismogenic depth starting at 25 km depth; b) stresses derived from the Kinematically Informed Heterogeneous Stress method; c) the combined regional and slip-driven stresses. The dynamic relaxation method contributes stress heterogeneities which encourage localized slip.

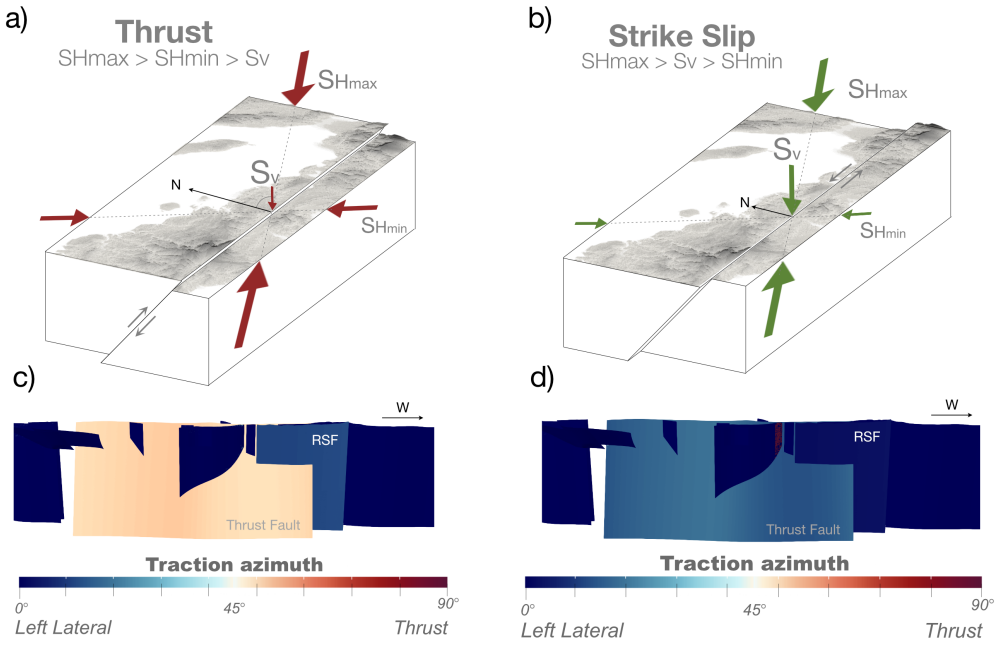

Figure 6: Schematic representation of regional stress tensors acting on a simple block model. The relative size of the principal stress components schematically with the topography of Haiti shown on the top face with a simple north-dipping fault schematically representing the TF: a) Schematic of a thrust faulting regime where the minimum horizontal component SH_{min} is larger than the vertical component, S_v; b) schematic of a strike slip faulting regime where the minimum horizontal component SH_{min} is smaller than the vertical component, S_v; c) corresponding shear stress direction in the thrust faulting regime with $\nu = 0.5$ resolved on the fault surfaces. This results in a higher angle of the traction vector (more thrust motion) on the north-dipping TF; d) corresponding shear stress direction in the strike slip regime with $\nu = 0.0$ resolved on the fault surfaces. This results in a shallower traction vector (mores strike-slip motion). Adapted from Heidbach et al. (2018)

resulting static stress change. As a result, parts of the fault which accumulated slip during the 2021 earthquake are assumed to have had pre-stress levels elevated beyond the background stress. This could be due to frictionally locked asperities, heterogeneities in the fault strength due to geology, or other conditions (Fig. 5b).

The Raimbault et al. (2023) GNSS and InSAR-derived static slip distribution is used to prescribe slip on the fault. For the numerical calculation, we first project the original Raimbault slip distribution onto the fault surfaces used in this study (which, although similar to the Raimbault et al. geometry, uses a new mesh). We taper the slip at the edges of the fault planes to prevent the generation of stress artifacts. We introduce artificial time dependence to the static slip distribution applying a Yoffe source time function to each slip vector on the faults (Tinti, Fukuyama, et al., 2005). We use a rise time of 1 second and a duration of positive acceleration of 0.1 seconds. We then impose this slip distribution with artificial time dependence as a boundary condition on the fault and allow the simulation to run resulting in what we call Kinematically Informed Heterogeneous Stresses. Because the slip rate fault is prescribed, in this method no assumptions are required about the dynamic traction direction (Tinti, Spudich, & Cocco, 2005; Tinti et al., 2021). After all seismic waves have dispersed, we calculate the final volumetric stress tensor at every point in the mesh and then smooth that volumetric field which still contains some artifacts from the courser discretization of the original Raimbault et al. slip model. We can then use the final stress state from this simulation in combination with regional stresses to describe a more realistic initial stress conditions on the fault. Kinematically Informed Heterogeneous Stresses are multiplied by a scaling factor, α (typically $0 < \alpha < 1$), which weights the Kinematically Informed Heterogeneous Stresses before being added to the regional stress tensor components.

3 Constraining the regional stress state

We seek to orient and scale the regional stress tensor to approximate the broad transpressional tectonic loading of the TF and RSF. The faulting regime in combination with the orientation of the principal horizontal stress component (SH_{max} orientation) and scaling of the principal stress components relative to one another (stress shape ratio, ν) determines the direction of traction (i.e. the direction of shear stress) resolved on the fault surfaces. Past modeling studies in this region have assumed a strike slip faulting regime (Douilly et al., 2015). The SH_{max} orientation for the 2010 earthquake has been estimated using GNSS block modeling and dynamic rupture modeling to be approximately $40-50^{\circ}$ (Calais et al., 2015, 2023; S. Symithe et al., 2015). However, these assumptions have not been tested for consistency with the 2021 earthquake rupture. Additionally, stress orientations are associated with large uncertainties, at best $\pm\ 15^{\circ}$ at the surface and $\pm\ 25^{\circ}$ at depth (Heidbach et al., 2018) and there may be significant variation across the peninsula (Calais et al., 2015).

Therefore, before developing any dynamic simulations, we first conduct a parameter exploration aimed at constraining the orientation and shape of the regional stress field in the vicinity of the 2021 rupture. To do this, we examine the impact of SH_{max} orientation and ν on the direction of traction resolved on the TF and RSF faults. If we assume that the direction of initial shear traction on a fault is parallel to the direction of slip (rake) during rupture, then we aim to find the range of regional stress conditions that produce traction aligned with rake observed during the 2021 earthquake. The rake and direction of traction are both defined according to Aki and Richards conventions (Aki & Richards, 1980) where 0° is pure left-lateral motion and 90° is pure thrust motion (Fig. 7). Slip distributions from inversion studies report the rake of the first sub-event to be greater than 40° (a combination of thrust and left lateral motion), while the rake of the second sub-event on the RSF is less than 30° (closer to pure left-lateral motion) (Calais et al., 2022; Li & Wang, 2023; Raimbault et al., 2023).

We resolve the average traction direction on the TF and RSF for a range of SH_{max} orientations from $30 - 70^{\circ}$ and ν values from 0.0 to 0.7, for both the case where $S_v > SH_{min}$ (thrust faulting regime) and the case where $SH_{min} > S_v$ (strike slip faulting regime). Fig. 7 shows the impact of SH_{max} orientation and ν on the direction of the average traction on the RSF and TF in the thrust faulting regime. In the thrust faulting regime, increases in the stress shape ratio, ν, result in a traction vector with a larger dip slip component, while clockwise rotation of the orientation SH_{max} reduces the dip slip component of the traction vector. Changing the orientation of the stress tensor, SH_{max}, also changes the direction of traction across the faults depending on the change in strike along the fault, but the effects are small ($\pm 5^{\circ}$, Fig. 7, Fig. S2). Traction direction on the RSF is less sensitive to parameter changes and remains less than 30° in most parameter combinations (Fig. 7). We find that in the strike slip faulting regime, the traction vectors generally have an insufficient components of dip slip to match observations. Even when $\nu = 0$ (the transition point between strike slip and thrust faulting regimes where $Sh_{min} = S_v$), the rake on the TF is only 15-20° (Fig S2). This case is explored more fully in the first dynamic rupture simulation (Model 2).

In addition to the alignment of the traction direction to the expected rake, we also consider how the choice of SH_{max} orientation and ν impacts the pre-rupture stress magnitude and strength of the fault. If, for example, stresses on the fault are not large enough to overcome the fault strength, then rupture cannot be sustained. We calculate the pre-stress ratio, R, across the fault surfaces, where higher R indicates that the fault is more likely to sustain rupture. We find that as the traction azimuth increases (closer to pure thrust motion), R tends to decrease (Fig. 4). R values are highest for low values of ν in the thrust-faulting regime.

We identify a range of values of ν and SH_{max} that balance agreement between the direction of traction within 15 degrees of the slip model rake while maintaining a high R value: we select values of ν between 0.2 and 0.5 and orientations of SH_{max} between 40-60° in the thrust faulting regime. In subsequent simulations, the modeled surface deformation reproduces the ratio of strike slip to dip slip motion implied by the InSAR data and GNSS observations, confirming this range of regional stress values.

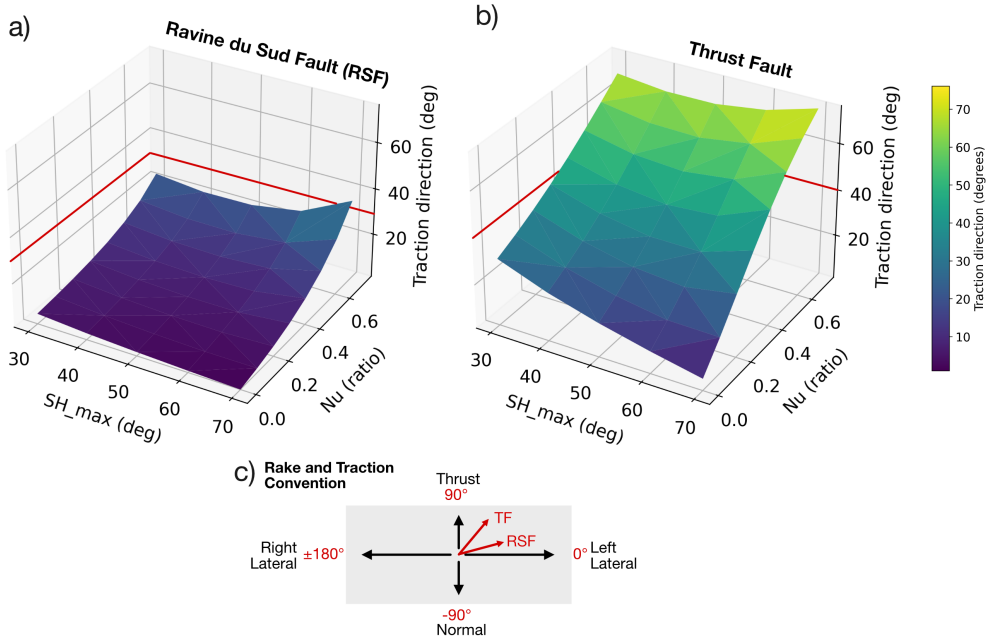

Figure 7: Plot showing the impact of SH_{max} and ν on the direction of the average traction vector on both the RSF and TF in the thrust faulting regime; a) on the RSF, the expected traction direction is less than 30° (shown with the red line); b) on the TF, the expected traction direction is greater than 40° (red line); c) schematic of Aki and Richards rake and traction direction convention.

Table 1: Table of parameters and definitions used in the dynamic rupture modeling setup.

Symbol	Parameter
D_c	Critical Linear Slip Weakening distance
μ_s	Static coefficient of friction
μ_d	Dynamic coefficient of friction
r_{crit}	Nucleation radius
α	Weight of Dynamic Relaxation stresses
R_0	Scaling of prestress ratio, R, for an optimally oriented virtual fault. Effectively scales regional stress magnitudes.
SH_{max}	Orientation of maximum principal stress component for regional stress tensor.
ν	Stress Shape Ratio
C_0	Frictional Cohesion

Table 2: Parameter values for the five dynamic rupture models discussed

Parameter	**Model 1**	**Model 2**	**Model 3**	**Model 4**	**Model 5**
D_c	0.03 m	0.05 m	0.06 m	0.06 m	0.02 m
μ_s	0.5	0.57	0.5	0.52	0.52
μ_d	0.15	0.5	0.16	0.16	0.16
r_{crit}	7 km	7 km	7 km	7 km	7 km
SH_{max}	40°	50°	40°	40°	40-50°
ν	0.5	0.0	0.5	0.5	0.0 - 0.5
R_0	0.4	0.4	0.4	0.4	0.14 - 0.41
α	0.0	0.0	0.9	0.9	0.7
C_0	3 MPa	3 MPa	3 MPa	3 MPa	2 - 5 MPa

4 Dynamic Rupture Modeling

4.1 Modeling Approach

Having identified a range of plausible regional stress parameters (SH_{max} orientation and ν), we now begin designing and running dynamic rupture simulations with the goal of better understanding the conditions which led to the observed 2021 rupture. Our approach for each suite of simulations is to begin with some assumptions about the initial conditions, then run and refine simulations, eventually producing a rupture most consistent with observations given the initial assumptions. By comparing the simulation outputs to key rupture observations, we learn more about rupture dynamics and can then update our assumptions about the initial conditions before running a new suite of simulations. In general, we aim to begin with the simplest assumptions and add complexity to the initial conditions only as needed.

For each simulation, we compare to six key observations and characteristics of the earthquake:

1. separation of strike slip and dip slip motion;
2. unilateral westward rupture;
3. rupture transfer from the TF to the RSF;
4. total moment magnitude (M_w7.2);
5. source time function (detailed below);
6. surface deformation observations (InSAR and GNSS, detailed below).

We compare to the source time functions from Calais et al. (2022), Goldberg et al. (2022), and Okuwaki and Fan (2022). Three InSAR interferogram pairs are used for comparison to model results. JAXA ALOS-2 interferograms are used because the L-band wavelength of this mission better captures large surface deformations in this highly vegetated region, especially in the near-fault region (Yin et al., 2022). Two ascending (A043 and A042) and one descending (D138) path interferograms covering the coseismic period are used from Yin et al. (2022). GNSS static offset data is taken from campaign data published in Raimbault et al. (2023).

In the following sections we present the results of five dynamic rupture simulations which each represent a major evolution in the initial condition assumptions. We address how each informed our understanding of the rupture dynamics of the 2021 earthquake and the conditions which may have led to it.

4.2 Model 1: Regional stress in the thrust regime

We begin with a simple dynamic rupture model where pre-rupture stress conditions across the fault system are defined by a single regional stress orientation and shape. We seek to determine if a single regional stress field, when applied to the assumed complex fault geometry, is sufficient to create dynamic rupture both on the TF and RSF with separated strike slip and dip slip motion. If sufficient, this would imply that the earthquake is primarily a result of the broad regional transpressive stress field in the presence of existing faults.

Based on the results from the sensitivity study in Section 3, this initial model imposes a regional stress tensor oriented at $SH_{max} = 40°$ and with stress shape ratio, ν= 0.5 in the thrust-faulting regime. We expect these conditions to create shear traction and therefore slip on the TF with an average rake of $\sim 51°$ and slip on the RSF with an average rake of $\sim 12°$ (Fig. 7), consistent with the expected rake from slip inversions. We vary the values of the remaining parameters to find a combination which sustains dynamic rupture beyond the forced nucleation zone but does not produce an unreasonably large earthquake (i.e. $< M_w = 7.4$). For this model, the parameters we find are $D_c =$ 0.03 m, $\mu_s = 0.5, \mu_d = 0.15$, $R_0 = 0.4$, and $C_0 = 3MPa$ at the surface. This results in a M_w7.39 earthquake, which produces slip on nearly the entire TF with an average rupture velocity of $\sim$ 3.5 km/s (Fig. 8a). There is a maximum of $\sim$2.5m of slip developing on the fault, which is comparable to estimates of peak slip from slip inversions. However, slip occurs over the entire extent of the TF, resulting in surface deformation that far exceeds that observed by InSAR and GNSS (Fig. 8c), and produces significant mismatch with the expected source time function (Fig. 8b). Importantly, this scenario fails to reproduce dynamic rupture transfer to the RSF, one of the key characteristics of this earthquake. We therefore conclude that a simple regional stress field does not result in the observed coseismic faulting pattern when all properties of the fault are assumed constant along-strike.

4.3 Model 2: Regional stress in the strike slip regime

In order to test which conditions are controlling the transfer of rupture from the TF to the RSF, we again impose a single regional stress tensor, but this time in the strike-slip faulting regime. We select the orientation $SH_{max} = 50°$ and stress shape ratio, ν = 0.0 (i.e. where $S_2 = S_3$), even though, based on the results in Section 3 (Fig. 7), we expect that this combination will result in slip on the TF with rake too shallow (i.e. not enough thrust motion) to match surface deformation observations. We again vary the values of the remaining parameters to find a combination which sustains rupture beyond the forced nucleation zone but does not produce an unreasonably large rupture ($< M_w =$ 7.4). We find that the following values achieve this balance: $D_c = 0.05$ m, $\mu_s = 0.57, \mu_d =$ 0.5, $R_0 = 0.4$, and $C_0 = 3MPa$ at the surface. Note the need to prescribe a relatively dynamically strong fault with a low strength drop ($\mu_s = 0.57$ and $\mu_d = 0.5$) in order to recreate the observed magnitude of slip. If the dynamic coefficient is decreased to make the fault dynamically weaker, then the peak slip on the fault increases to produce unreasonably large earthquakes.

After nucleation, the rupture propagates bilaterally on the north-dipping TF. After approximately 17 seconds of rupture time, nearly the entire TF has slipped on the order of 1 m. The rupture front to the west reaches the termination of the TF, $\sim$15 km west of the intersection with the more steeply dipping RSF. Despite the geometric barrier formed by this intersection at about $\sim$14 km depth, dynamic rupture successfully transfers to the RSF almost immediately. The final moment magnitude of the earthquake is M_w 7.23, close to the observed moment magnitude of M_w7.2. However, the maximum slip of $\sim$1.4 m is smaller than the expected $\sim$2.3 m and remains relatively constant across the TF and RSF.

In this model, like Model 1, slip on the TF extends over the entire fault as opposed to the expected compact rupture centered around 73.6°W (Fig. 9a). This results in a broad first moment rate peak inconsistent with STF estimates (Fig. 9b) and does not reproduce inferred troughs and multiple peaks in the source time function. Two to three pulses of slip are inferred in many past studies of the 2021 earthquake, including back-projection results (Okuwaki & Fan, 2022) and joint teleseismic inversion studies (Goldberg et al., 2022), which indicates that there is at least one delay in moment release which is important to recreate (Fig. 9b).

Slip on the TF has a rake of ∼16-18° and slip on the RSF has a rake of ∼2-3°, closer to pure strike slip motion (Fig. S2). While this change in rake between the TF and RSF reproduces the separation of strike slip and dip slip motion, it fails to produce sufficient thrust motion on the TF to match observations, estimated from slip inversions to be 40+° (Fig S2). The descending LOS image shows this mismatch (Fig. 9c), where the observed LOS shows a lobe of positive deformation (consistent with uplift) north of the TF surface trace, whereas the simulated LOS deformation remains negative north of the TF surface trace (Fig. 9c, RMS = 0.122). This comparison illustrates that the vertical motion produced by the TF in this simulation must be larger relative to the left lateral motion in the LOS direction to agree with InSAR observations. Producing dynamic rupture transfer coupled with sufficient thrust motion on the TF is difficult with a single regional stress field because the regional stresses required to produce enough thrust motion on the TF to match the observations, tend to result in very low pre-stress levels on the RSF (i.e. low R). This is shown in Fig. 4, which compares the initial values of R resolved on the fault surfaces for Model 1 and Model 2. Model 1, which produces the correct rake on the TF has near-zero R values on the RSF, which explains why it does not rupture easily. Model 2, which produced rupture transfer but insufficient dip slip motion on the TF with high R values on both TF and RSF (reaching up to R=0.37 for Model 2, versus maximum R=0.14 for Model 1, Fig 4). Regardless of the faulting regime, both Model 1 and Model 2 simulations with a single regional stress tensor produce an extended duration and length of rupture on the TF that is not consistent with the observations.

This simulation illustrates that the stress shape ratio ν is a key factor controlling the transfer of rupture from the TF to the RSF. Therefore, some along-fault variation in the initial stress and strength state or the shape and orientation of the regional stress tensor may be contributing rupture transfer and the compact nature of the resulting slip patches.

4.4 Model 3: Combined Regional and Kinematically Informed Heterogeneous Stresses in the Thrust Regime:

It is impossible to know the true initial stress state on the fault surfaces prior to the earthquake. However, we can carry out an experiment to see how initial stress heterogeneity may influence the dynamic rupture. In Model 3, we introduce stress heterogeneity on the faults determined from a static slip model (Raimbault et al., 2023) using a Dynamic Relaxation simulation (Sec.2.4.2). The introduction of these stresses adds variation to the background regional stress resolved on the fault surfaces (see Methods section).

We expect that dynamic slip will concentrate more compactly on parts of the fault with higher initial stress, and may encourage rupture transfer onto the RSF due to elevated stress on the RSF where slip is expected. For this simulation, we chose a regional stress field oriented with $SH_{max} = 40°$ and ν= 0.5 in the thrust faulting regime. We weight the Dynamic Relaxation-derived stresses using α=0.9. Given these conditions, the combination of parameters which sustains rupture but produces a $< M_w = 7.4$ event is: $D_c = 0.06$, $\mu_s = 0.5$, $\mu_d = 0.16$, $R_0 = 0.4$, and $C_0 = 3MPa$ at the surface.

After nucleation, the TF ruptures away from the hypocenter bilaterally. Within 20 seconds, the western rupture front has reached the intersection with the RSF but fails to transfer. By 30 seconds it has ruptured the entire extent of the TF. However, unlike previous ruptures, in this simulation slip concentrates in patches near the center of the TF (∼73.6°W), with a peak slip of ∼2.4 m which decreases away from the center of the fault (Fig. 10a) and final moment magnitude M_w7.31. This results in better agreement with the InSAR data, where deformation is concentrated over the observed coseismic region (Fig. 10c). However, the entire TF still ruptures, creating disagreement with the extent of deformation in the InSAR observations (where the simulation creates surface deformation which extends further to the east and west compared to the observations) and the width of the single moment rate peak (which is much wider when compared to the observations, shown in Fig. 10b). The combination of rupture transfer from the TF to the RSF with 40 + rake on the TF remains elusive.

Model 3 illustrates that initial stress heterogeneity can act to concentrate slip at particular locations on the fault but does not appear to control the extent of rupture, nor is it alone sufficient to transfer rupture from the TF to the RSF.

4.5 Model 4: Introducing fault strength variations

When constructing the fault geometry, we purposely extended the TF fault past the limits of the observed rupture in order to understand what factors influence the extent and location of rupture (Fig. 2). In all experiments to this point, slip on the TF extended to the limits of the fault specified in the geometry, well beyond the actual rupture. It was also difficult to reproduce the timing of the rupture transfer from the TF to the RSF. In this experiment, we introduce heterogeneities in the along-fault frictional properties on the TF to investigate whether a change in fault properties that limits slip to the east and west could be influencing rupture transfer to the RSF and the extent of slip. We note that, due to dynamic-trade-offs, choosing an increased mu_s may also be a proxy for locally lower initial shear stresses, e.g., reflecting stress shadows of previous regional earthquakes (e.g., Taufiqurrahman et al., 2023), or unmodeled changes in fault geometry. What we represent in this model as changes in fault strength could alternatively represent termination of the TF or changes to the strike or dip of the TF structure at these locations.

The InSAR data (the main observation indicating the rupture extent) shows minimal surface deformation close to the mapped EPGF approximately east of 73.4°W (point Y in Fig. 1b) and west of 73.8°W (point X in Fig. 1b) (Fig. 12c). In Model 4, we increase the static fault strength (μ_s) to 1.0 east and west of these locations to discourage rupture propagation. We otherwise leave $\mu_s = 0.52$ as in previous simulations. The extent of these static strength changes are shown in Fig. 12d. All other parameters are identical to the previous simulation (Model 3).

After nucleation, the dynamic rupture propagates on the TF, however, instead of rupturing bilaterally as in previous simulations, the rupture front quickly encounters the increased static strength of the fault to the east (east of point Y on Fig. 1b), limiting slip extent. To the west, after about 15 seconds, the rupture front encounters increased static strength west of point X (Fig. 1b), limiting the rupture. Despite the rupture propagating past the beginning of the intersection with the RSF, it does not transfer to the RSF fault. The limitation of the spatial extent of the slip on the TF creates a compact rupture that reproduces the surface deformation pattern in the eastern part of the rupture (Fig. 12c). These increases in fault strength also result in a narrower moment rate pulse which more closely resembles the first peak of the Goldberg et al. (2022) source time function (Fig. 12b). The maximum slip is ∼2.3 m, similar to the Raimbault et al. (2023) slip distribution, and the limited lateral extent of slip means that the moment

magnitude of the rupture is smaller, M_w7.10. This is less than the observed M_w7.2 rupture but that is expected given the non-rupture of the RSF.

We find that the lack of rupture propagation from the TF to the RSF is a persistent feature of all ruptures which assume a thrust faulting regime with a high stress shape ratio (ν =0.3 - 0.5, not all simulations shown). This remains true even when the strength of the RSF is reduced, and when the pre-stress levels on the RSF are increased (achieved by increasing R_0). The lack of RSF rupture in the Model 4 simulation is evident in the mismatch between the simulated and observed InSAR data (Fig. 12c). The simulated InSAR data produces no surface rupture on the RSF as opposed to what is observed in track A043 (RMS=0.276). We also note the lack of multiple moment rate peaks in the source time function (Fig. 12b) and that there is a mismatch at the two GNSS sites, CAMR and CAMY, just south of the RSF (Fig13a). GNSS vectors very close to a fault are often difficult to match exactly, for example due to fault fling (e.g. Calais et al., 2010). The fit to stations CAMR and CAMY might be improved by further refining the details of the western termination of the RSF. Despite the non-rupture of the RSF, the lobe of uplift which is readily apparent in the Descending InSAR Scene is reproduced by the increased shear strength of the eastern portion of the TF (RMS=0.079). The simulated GNSS data surrounding the rupture on the TF demonstrates a close match to the observed data (Fig. 12a).

Model 4 demonstrates that changes in friction along the TF is one way to implement along-strike variations in fault properties and effectively limits the rupture extent.

4.6 Model 5: Combined Regional and Kinematically Informed Heterogeneous Stresses with Lateral Variation in Regional Stress Field

In all previous simulations in the thrust faulting regime, dynamic rupture did not transfer to the RSF. The following experiment tests the hypothesis that an along-strike change in the regional stress field would favor rupture transfer while preserving the large amount of dip slip motion on the TF.

We combine the stress conditions that produced rupture transfer from the TF to the RSF in Model 2 and the conditions which produced sufficient thrust motion on the TF in Model 4. To do this, we set $SH_{max} = 50^{\circ}$, $\nu = 0.0$ on the RSF and $SH_{max} = 40^{\circ}$, $\nu = 0.5$ on the TF, both in the thrust faulting regime. We calibrate the value of R_0 individually on each fault to ensure reasonable slip on both segments, using $R_0 = 0.14$ on the RSF and $R_0 = 0.41$ on the TF (and all other faults). We lower R_0 to 0.14 on the RSF to prevent slip from becoming too large after rupture transfer. In this simulation we also increase the frictional cohesion (C_0) near the surface on the TF to 5 MPa to better reproduce the smooth transition across the TF without obvious surface rupture. We decrease the frictional cohesion near the surface on the RSF to 2 MPa to better reproduce the sharp surface rupture across the RSF observed in the InSAR data (Fig. 14). We find that there is only a very narrow range of parameters that both allow rupture propagation to the RSF but generate a reasonable slip magnitude on the RSF. We ultimately find an appropriate combination of parameters: $D_c = 0.02$, mu_s= 0.52, mu_d=0.16, $\alpha = 0.7$.

This rupture, like Model 4, begins with largely unilateral rupture to the west. After about 10 seconds, the rupture reaches the intersection between the RSF and TF (Fig. 11d) and soon after encounters increased static friction west of point **U** (Fig. 15). Here, the rupture almost stops but eventually begins to slip at the intersection between the RSF and TF. The rupture on the RSF slips slowly at first, then accelerates toward the surface of the RSF. Slip on the RSF has rake ranging between ∼40-60°, and slip on the TF has rake ranging between ∼0-30°. This period where the rupture encounters the intersection of the RSF and TF corresponds to the trough in the source time function expected from the teleseismic data at about 10 seconds (Calais et al., 2022; Goldberg et

al., 2022; Okuwaki & Fan, 2022). Additional source time functions are included for comparison in Fig. 14b to show the variability inherent in moment rate release estimates.

Several additional simulations which are not shown adjusted the location of 'point **T**' (Fig. 12) where static friction increase begins, to better understand its relationship to rupture transfer, timing, and fit to the InSAR data. We find that when introducing an increase in μ_s on the TF further to the west, rupture extends further to the west before transferring to the RSF. This is inconsistent with the InSAR data which indicates that there is no subsurface rupture that far west. When the μ_s on the TF increases west of point **T**, we find that the rupture transfers more quickly to the RSF, resulting in a better fit to the moment rate and better fit to the InSAR data. Even with these adjustments, there is still some disagreement with the InSAR data at the western edge of the TF, west of point **X** (Fig. 14c and 13b). We find that it is difficult to reproduce the concentrated slip near the surface on the RSF which is observed in the InSAR data. This remaining discrepancy causes some misfit between the modeled surface deformation and the InSAR and GNSS data near the Ravine du Sud fault (Fig. 14c, RMS=0.213 for A043, RMS=0.093 for D138). However, the simulated rupture from Model 5 has otherwise strong agreement with all observations: InSAR surface deformation, GNSS offsets, and source time function. It also reproduces all of the key characteristics of the earthquake: separation of strike slip and dip slip motion on two separate fault planes, rupture transfer to the RSF, and source time function.

The main result is therefore that a significant change in the regional stress field is necessary to produce the observed slip on the RSF in our fault geometry as well as some variation in along-strike dynamic parameters such as fault strength.

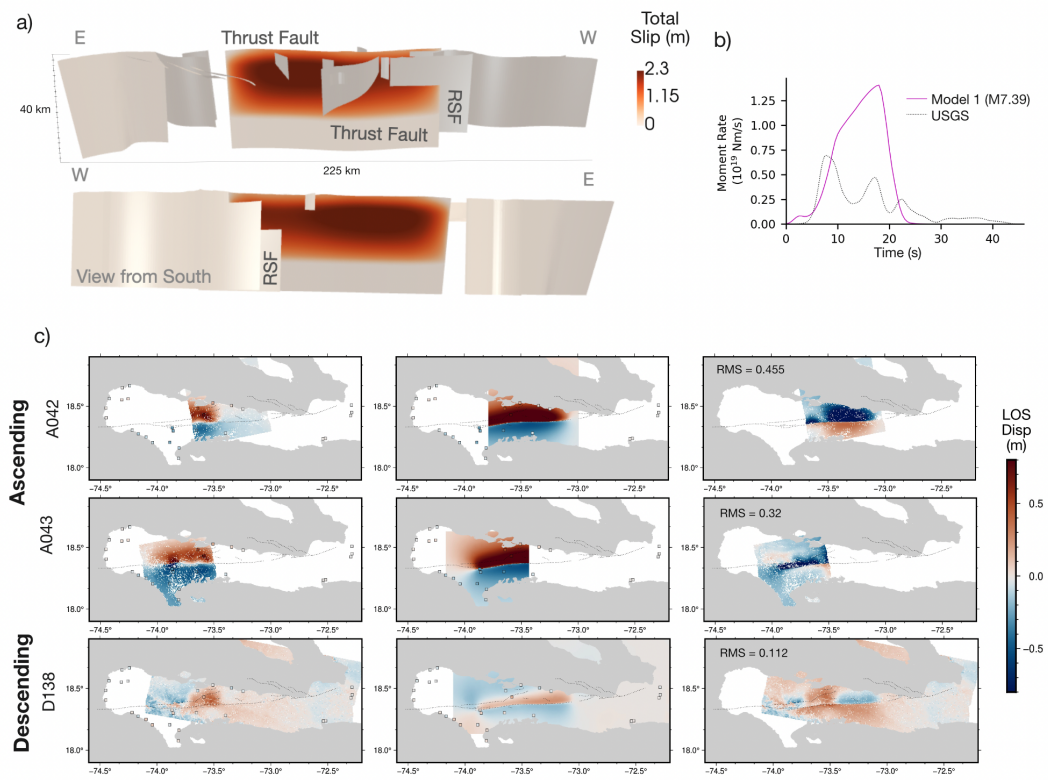

Figure 8: Summary of results from Model 1: Regional stresses in the thrust regime a) Final slip distribution. Slip is distributed evenly over the entire TF, no rupture transfer to the RSF; b) source time function comparison between the Goldberg et al. (2022) model (grey) and this model (purple). Overall rupture moment magnitude is too large and there are no distinct pulses, unlike the Go23 source time function; c) Observed InSAR data from ALOS-2 tracks A042, A043, an D138 compared with simulated LOS surface deformation data. Overall magnitude of surface deformation is too large, creating a large misfit in pattern andmoment magnitude between the modeled deformation and observed deformation, seen as large residuals.

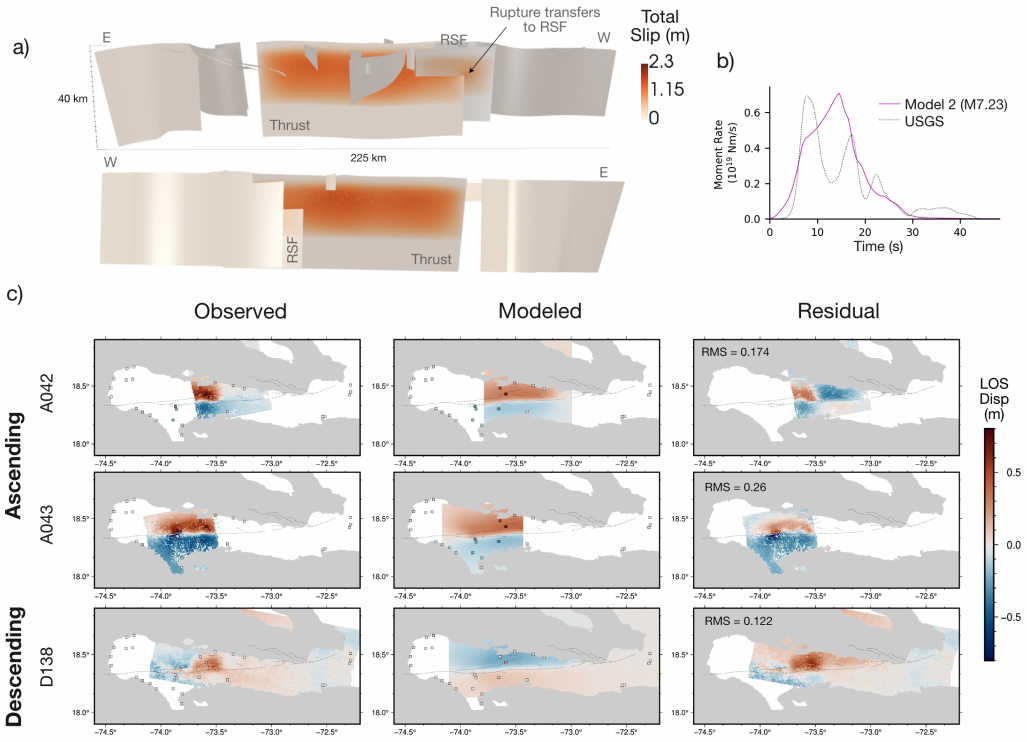

Figure 9: Summary of results from Model 2: regional stresses in the strike slip faulting regime: a) Final slip distribution for Model 2. Slip is distributed evenly over the entire TF and rupture has propagated to the RSF with significant slip; b) source time function comparison between the Goldberg et al. (2022) model (grey) and this model (purple). Overall rupture moment magnitude is captured but without distinct peaks, unlike the Go23 source time function; c) Observed InSAR comparison with simulated LOS surface deformation data. Amplitude of residuals is decreased with respect to Model 1, however there remains a strong misfit in the pattern between the modeled deformation and observed deformation. The descending pair (D138) shows negative deformation in the LOS direction of the observing satellite whereas we expect a lobe of positive deformation from strong thrust motion the TF as seen in the observed interferogram. This indicates the stress orientation plays a role in producing later slip on the RSF which contributes to creating a peak later in the source time function.

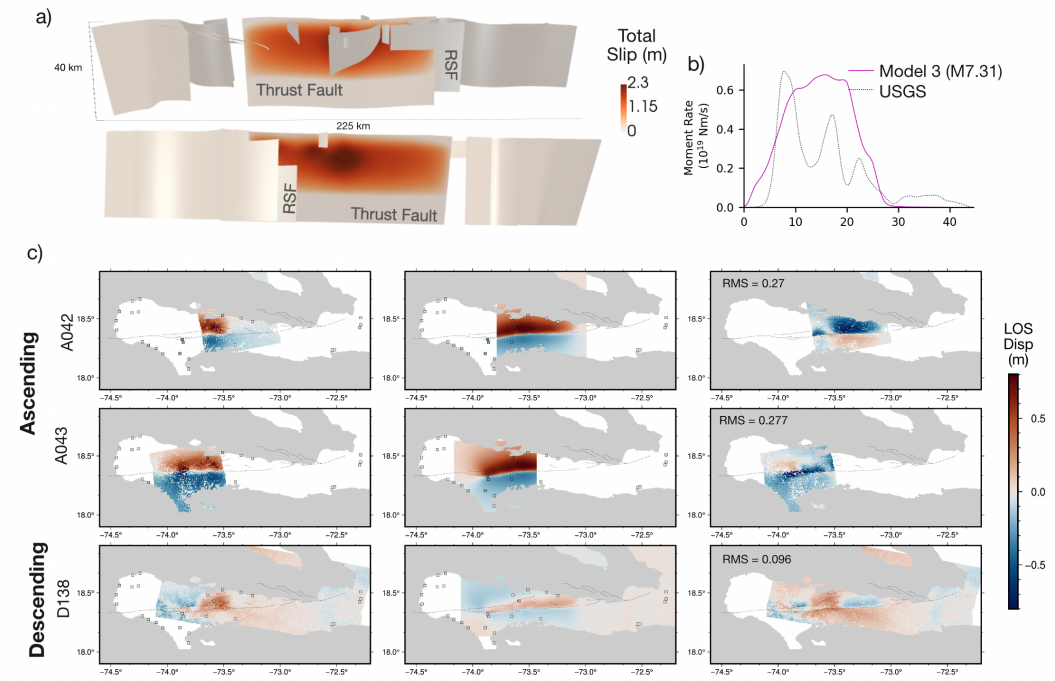

Figure 10: Summary of results from Model 3: Combined regional and dynamic relaxation (DRT) stresses in the thrust regime a) Final slip distribution for Model 3. While slip still extends over the entire length of TF, slip concentrates near the center of the fault. There is no rupture transfer to the RSF; b) source time function comparison between the Goldberg et al. (2022) model (grey) and this model (purple). The peak of the source time function is roughly the right amplitude but there are no distinct peaks and the single peak is too wide; c) Observed InSAR data from ALOS-2 tracks A042, A043, an D138 compared with simulated LOS surface deformation data. Overall magnitude of surface deformation remains too large, but uplift, seen as a red lobe in the simulated track D138 data, is broadly reproduced. This indicates that concentrating the dip-slip motion in lateral extent is important for reproducing the InSAR pattern with dip-slip dominating strike-slip motion in the surface deformation.

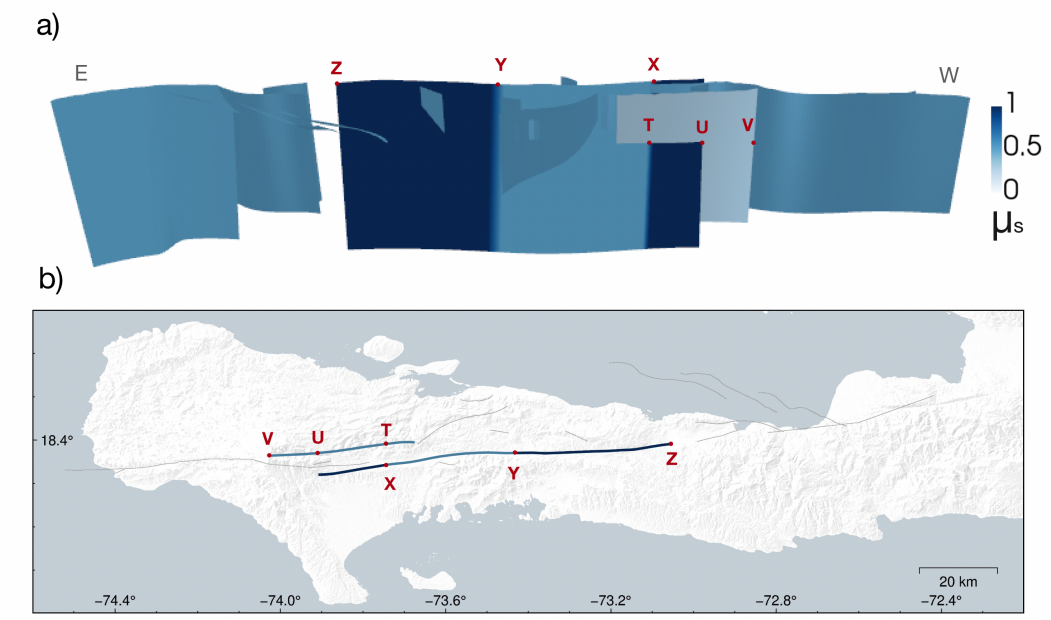

Figure 11: Variable static coefficient of friction on the fault surfaces. This distribution of μ_s is used in both Model 4 and Model 5. Points of interest T, U, V, X, Y, and Z are shown in red.

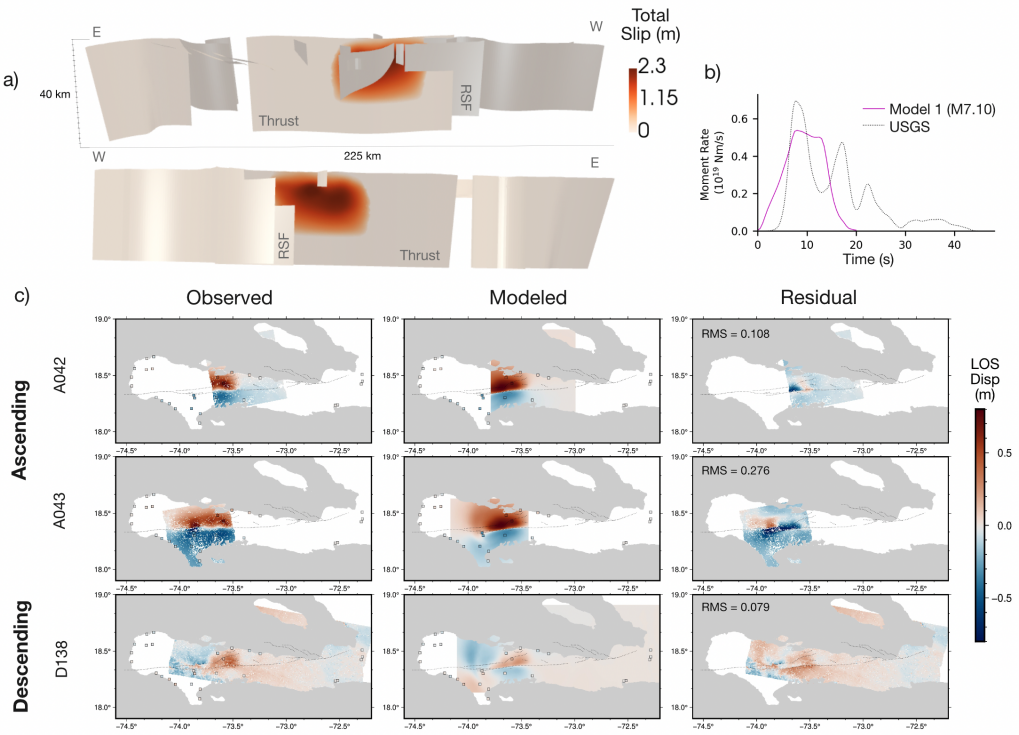

Figure 12: Summary of results from Model 4: combined regional and DRT stresses in the thrust faulting regime with fault strength variations: a) Final slip distribution for Model 4. Slip patches are more compact than in Model 2, but there is no rupture transfer and therefore no slip shown on the RSF; b) source time function comparison between the Goldberg et al. (2022) model (grey) and this model (purple). Overall moment magnitude is captured but there are no distinct peaks in the source time function, unlike the Go23 model; c) Observed InSAR comparison with simulated LOS surface deformation data. Modeled surface deformation data closely matches the observations in amplitude and pattern. In particular, the synthetic descending LOS deformation (D138) shows a lobe of positive deformation in the LOS direction of the observing satellite which agrees with the observed interferogram. This indicates that a limited rupture extent on TF contributes to matching the pattern of uplift;

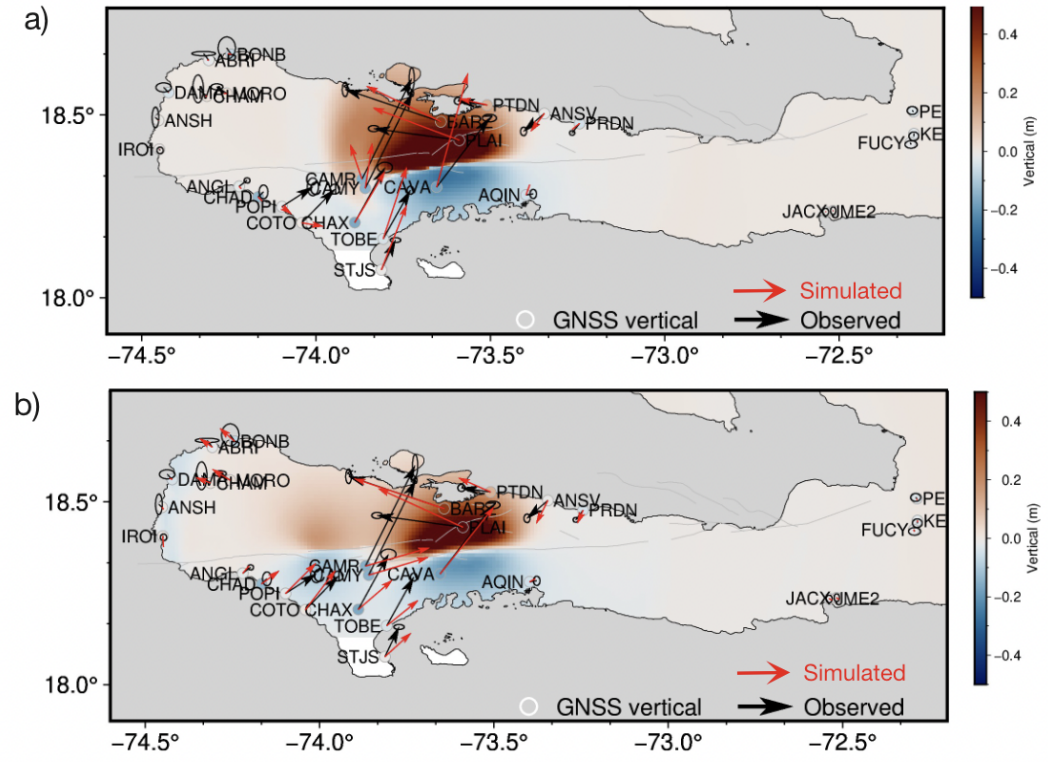

Figure 13: Comparison between observed GNSS coseismic offsets (horizontal deformation shown with black arrows, vertical deformation shown by color of circles) and simulated offsets (horizontal deformation shown with red arrows, vertical deformation shown as the background gridded red/blue data). a) Model 4 comparison; b) Model 5 comparison.

5 Discussion

5.1 Interpretation of the Thrust Fault

One important unresolved question about the 2021 earthquake is the relationship of the Thrust Fault to the previously assumed vertical EPGF (Prentice et al., 2003; Saint Fleur et al., 2020). The same question was asked about the 2010 Léogane fault. The fault system geometry has major implications for understanding how this margin accommodates transpression. The Thrust Fault used in our model roughly follows the trace of the EPGF (Saint Fleur et al., 2020), and continues at depth dipping 66°N, constrained such that it roughly follows the aftershock locations (Douilly et al., 2023). The fault is represented as a single, nearly planar feature as in Raimbault et al. (2023). The ability of Model 5 to reproduce observations of the 2021 event suggests that the TF geometry with our proposed modifications represents one possible geometry.

As more detailed aftershock locations became available (Douilly et al., 2023), they suggested that at depth this fault is likely not planar but can instead be interpreted as two or three planes that more closely follow aftershock clusters. This kind of variation of fault strike could also terminate of limit the extent of fault rupture, which we reproduced by varying fault friction. There is also a small subset of aftershocks that lie in a vertical plane below the EPGF fault trace east of the rupture that may indicate the presence of a separate EPGF (Fig 1). In this conception, the vertical EPGF would produce the persistent topographic features observed and, over geologic time, would take up the motion of a larger earthquake.

It remains unclear if this north-dipping fault, whether comprised of a single planar segment or multiple segments, is itself the EPGF or a parallel strand running alongside the vertical EPGF. The possibility of two parallel faults with different dips has different implications for understanding the long-term accommodation of strain across the peninsula.

Designing new meshed fault geometries would be an important undertaking for expanded dynamic rupture modeling experiments to help address these different hypotheses. This study serves as a guide for the level of detail and scope of simulations that could supplement such future studies.

The results of our modeling suggest that the TF we proposed is subject to transpressive regional stresses which are most closely approximated by a thrust-faulting stress regime with a stress shape ratio ν=0.5 on this fault. Recent GNSS work from Calais et al. (2023) proposed two possible block models in which shortening is either accommodated almost entirely by the Jeremie-Malpasse thrust fault off the north-shore of the Tiburon peninsula or an alternative model where compression and strike slip motion are both accommodated along the EPGF. Our model results support the interpretation that significant shortening is acting as far south as the mapped EPGF, as opposed to being entirely accommodated by offshore thrusts, like the Jeremie-Malpasse fault to the north (Calais et al., 2023).

Including significantly longer fault segments in the model than actually ruptured in the main earthquake led to several challenges in reproducing the observed behavior. However, it also led to a more in-depth understanding of the controls on fault rupture. For example, had we made the assumption in advance that the TF terminated at the start of the RSF then rupture would likely have transferred to the RSF without an investigation of the many factors that control that transfer.

5.2 Unruptured Miragoâne Segment

The Thrust Fault was designed to extend from Massif Macaya all the way to Lake Miragoâne (Fig. 1) and dips 66°N. This distance is considerably longer than the extent

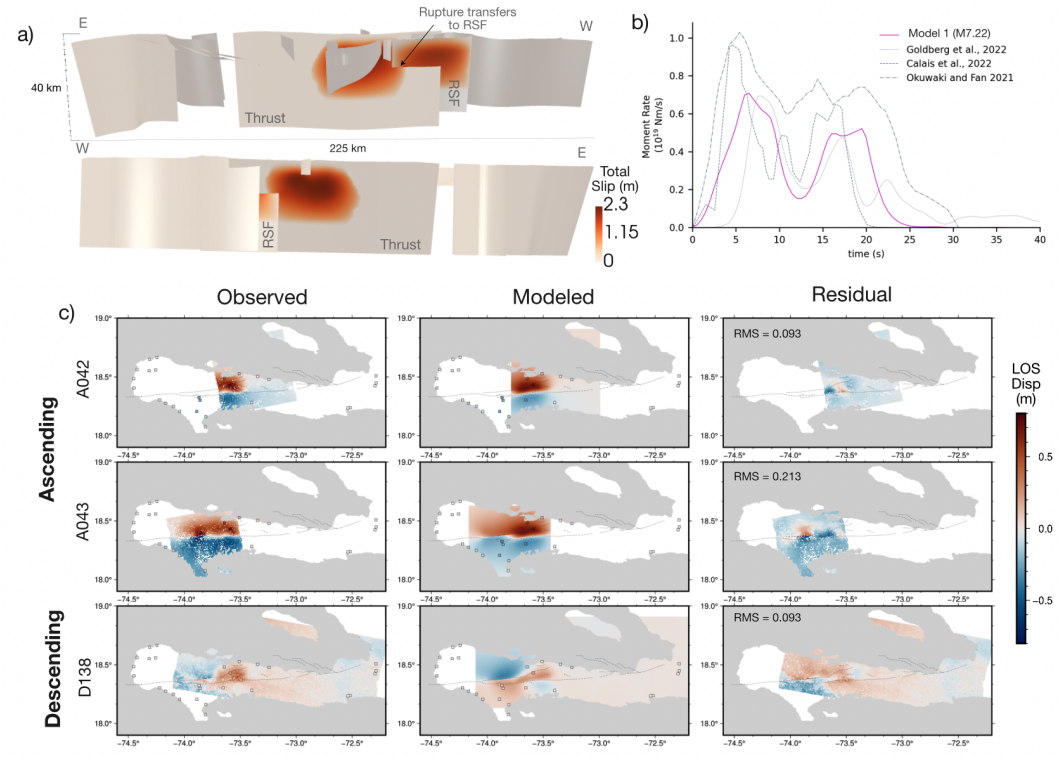

Figure 14: Summary of results from Model 5: Lateral variations in regional stresses combined with DRT stresses and fault strength variations: a) Final slip distribution for model 5. Slip patches concentrate compactly on the TF and RSF, where slip on the RSF indicates successful rupture transfer b) source time function comparison, this time with expanded comparisons between Calais et al. (2022), Goldberg et al. (2022), and Okuwaki and Fan (2022) (grey) and this model (purple), where there is good agreement in the moment magnitude and timing, and where the two distinct peaks in the source time function correspond to the rupture transfer from TF to RSF; c) Observed InSAR comparison with simulated LOS surface deformation data. Modeled surface deformation data closely matches the pattern and amplitude of the observations, with the synthetic descending LOS deformation (D138) showing the expected lobe of positive deformation in the LOS direction. The deformation now matches the InSAR deformation in the narrow region between the RSF and TF.

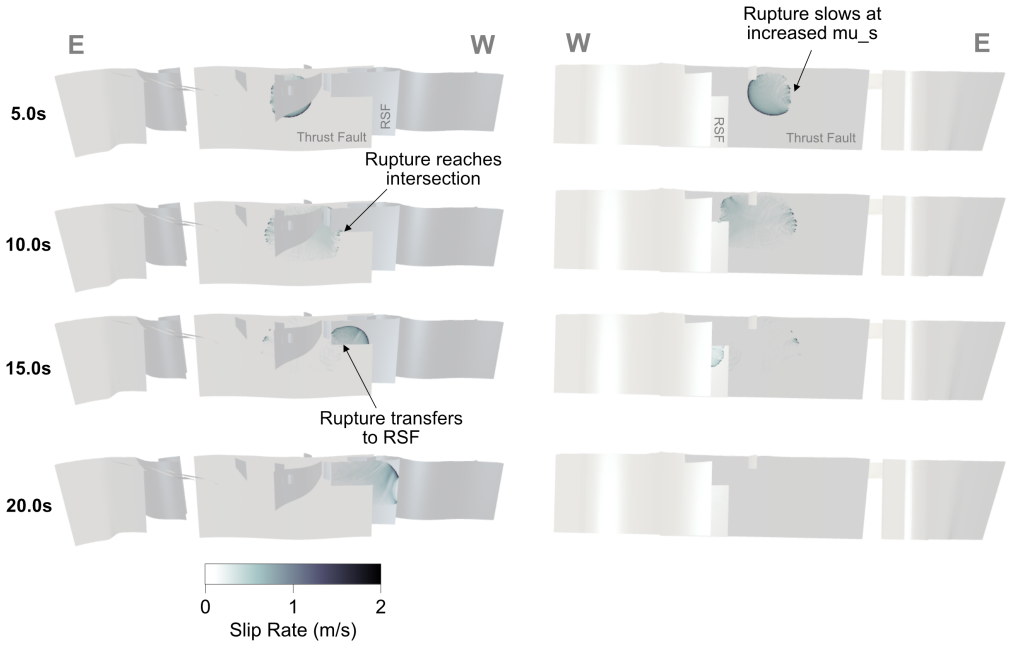

Figure 15: Snapshots of absolute slip rate for Model 5. Left column shows a view from the north and right column shows a view from the south. Rupture nucleates on the TF, at 10 s reaches the intersection with the RSF where the slip rate decreases before, at 15 sec, rupture transfers to the RSF and slip rate increases as the rupture propagates upwards before terminating at around 20 sec.

of the known rupture from InSAR data (Fig. 1b). From the Basin of L'Asile to Lake Miragoâne, we increase the static friction coefficient in Models 4 and 5 in order to terminate rupture where surface deformation becomes negligible in the InSAR data. Increasing μ_s or decreasing initial shear stresses locally to terminate rupture is a common approximation used in dynamic rupture modeling, particularly when using a LSW friction law, where there is no mechanism to account for velocity-strengthening rheology of the fault that may decelerate dynamic rupture (e.g., Galis et al., 2019). The segment of the EPGF between the 2010 and 2021 ruptures is puzzling because both earthquakes were estimated to have increased the Coulomb Failure Stress here (Calais et al., 2022; S. J. Symithe et al., 2013). Interestingly, the west and the east ends of this unruptured segment also slipped shallowly in the weeks following the 2010 and 2021 earthquakes, respectively (Wdowinski & Hong, 2012; Yin et al., 2022). It is critical to understand whether this segment is locked and highly hazardous, or whether it is accommodating strain differently than the surrounding segments.

One explanation could be that the the eastern edge of the 2021 rupture simply marks the end of the TF where it intersects with the vertical EPGF. This change in geometry could prevent the propagation of the rupture onto the unruptured segment. This interpretation is supported by the change from north-dipping to vertical clusters of aftershock seismicity east of the rupture (Douilly et al., 2023). A change in fault dip could also make rupture transfer less dynamically feasible, as we showed was the case for the rupture transfer between the north-dipping TF and vertically-dipping RSF, which would explain the eastern termination of the rupture. Another possibility is that the unruptured segment is relatively weak and, for example, creeping at depth such that there is little stress remaining to be released to continue the rupture. . However, the GNSS velocity transects across the fault do not indicate interseismic creep (Calais et al., 2015), nor does recent interseismic InSAR analysis (Raimbault, 2023). A third possibility is that this segment ruptured most recently (i.e. 1770, Hough et al., 2023) and stress has not yet recovered.

5.3 TF West of the 2021 Rupture

In Models 4 and 5, we increase the static coefficient of friction west of the rupture as seen in the InSAR. Increasing the static fault strength of this section was required to match the InSAR surface deformation field and GNSS coseismic offsets and reproduced the timing of the first trough in the modeled source time functions (Calais et al., 2022; Goldberg et al., 2022; Okuwaki & Fan, 2022). The dynamic rupture models demonstrated a need to increase the static strength of the west end of the TF that is parallel to the RSF in order to reproduce the observations. This suggests that, while at one point this may have been an active strand of the EPGFZ or part of a flower structure, it is either no longer active or the north-dipping TF ends before this section begins.

Here and for the east end of the TF, the change in frictional properties can be considered a proxy for fault characteristics or features that change that location. The change in characteristics means that segmentation is important, however as the two earthquakes in 2010 and 2021 showed, it cannot be easily interpreted from surface features in advance. This presents challenges for earthquake hazard estimates that include a recurrence model for characteristic earthquakes based on fault length (Wells & Coppersmith, 1994). A statistical approach that accounts for different potential rupture lengths (e.g. Field et al., 2014) is necessary.

5.4 Strain Partitioning at the EPGF

The oblique relative motion between the North American and Caribbean tectonic plates creates transpression across Hispaniola. However, there is ongoing debate about how that transpression is accommodated and partitioned among fault systems. While the Enriquillo-Plantain Garden Fault Zone (EPGFZ) has historically been understood

to be a vertical fault accommodating only left lateral motion, recent geodetic work, recent re-examination of historical events, and oblique focal mechanisms in the recent 2010 and 2021 earthquakes supports the interpretation that significant crustal shortening and thrust faulting reaches as far south as the EPGF. The partitioning of strain across the region plays a critical role in our understanding or earthquake hazard and risk in Haiti (S. Symithe & Calais, 2016). Recent block modeling of GNSS data proposed two competing block models for this region, but the observations cannot easily distinguish between the two models (Calais et al., 2023).

The historical earthquakes in 1701, 1770, and 1860, were assumed to be strike slip earthquakes which occurred on the EPGF (Bakun et al., 2012). Some have used this to suggest a multi-rupture mode for this plate boundary which alternates between strike slip events on the EPGF and thrust events on secondary faults over the course of centuries (Wang et al., 2018). However, (Hough et al., 2023) recent re-examination of the 1770 and 1860 events, suggests that these events could have occurred on partially on oblique thrust faults (Hough et al., 2023; Martin & Hough, 2022). This, combined with the knowledge of the 2010 and 2021 events both initiating on north-dipping unmapped thrust faults, suggests that perhaps significant thrust motion is a typical mode of failure for this fault zone. Despite significant geologic field work and other geophysical data collection over the last several decades, there is still high uncertainty in the fault dip through much of the peninsula. Perhaps fault segmentation includes sections of vertical strike slip fault (like the unruptured section) while other sections prefer oblique thrusting. This work supports the interpretation of combined thrust and strike slip motion and adds the constraint that this implies variation in the stress tensor along the plate boundary.

6 Conclusions

3D dynamic rupture modeling experiments were used to test which conditions may have contributed to the complex 2021 M_w7.2 Haiti earthquake rupture. We developed a highly complex fault geometry which included two main coseismic fault surfaces: a north-dipping Thrust Fault (TF) and a near-vertical Ravine du Sud Fault (RSF), as well as a detailed network of surrounding fault segments that allowed potential rupture over a much larger extent than was observed. The dynamic rupture models were tested against the following observations and characteristics: M_w7.2 moment magnitude, a multi-peak source time function, rupture transfer to the RSF, and spatial separation of dip slip and strike slip motion. This characteristic separation of dip slip and strike slip motion is observed in the InSAR deformation pattern and confirmed by GNSS where vertical motion dominated over left lateral motion in the LOS direction.

Results indicate that regional stress shape and orientation were key influences on both the orientation of slip (rake) and the transfer of dynamic rupture from the TF to the RSF. Regional stress with orientation SH_{max}=40° and ν=0.5 produced shear stress resolved on the TF that best aligned with the surface deformation observations. However, a dynamic rupture model using this simple description of regional stress (Model 1) did not produce the observed slip on the RSF, which suggested that a more complex system was required. While stress heterogeneities localized the simulated slip in closer agreement with the observed surface deformation pattern, they did not impact the lateral extent of rupture or the rupture transfer to the RSF. Changing the assumed orientation of the stress tensor and the stress shape ratio between the RSF and TF faults was required to produce transfer of the rupture to the RSF and to produce shear stresses on the RSF oriented in agreement with the observed rake.

Along-strike variations in fault friction on the TF were key to focusing the slip to the observed geographic patches and producing narrow, distinct peaks in the source time function. The change in frictional properties can be considered a proxy for fault characteristics or features that changed at that location, for example a change in orientation

or termination of the fault. The change in along-strike characteristics means that segmentation is important, however as the two earthquakes in 2010 and 2021 showed, it cannot be easily interpreted from surface features in advance. In fact, the segmentation proposed in Saint Fleur et al. (2020) does not represent conditions that can lead to a dynamic rupture model that reproduces the observed characteristics.

Combining regional stress changes with along strike variations in fault friction created a major slip patch on the TF along with dynamic rupture transfer to the RSF with the right timing to reproduce the source time functions. This simulation (Model 5) best fit all of the observational datasets. These results assume the dynamic rupture of a thrust fault with 66°N dip. However, this does not preclude the existence of a parallel vertical EPGF, nor does it test any variations in the assumed rupture geometry. Future dynamic rupture modeling efforts may be used to explore how variations in the defined fault rupture geometry may have impacted the dynamic rupture evolution.

The variability in local stress regime and fault strength implied by the dynamic rupture modeling results suggests that any of the minor or unmapped compressional fault features or strike slip segments located within this highly deformed compressional microplate boundary may be candidates for releasing accumulated strain. More work is needed to understand how this fault zone is accommodating tectonically driven stresses. Recent efforts to map and categorize surrounding faults (Calais et al., 2023; Saint Fleur et al., 2020, 2024) and monitor their microseismic activity (Calais et al., 2022; Douilly et al., 2023) will contribute to these ends.

7 Data and Resources

All data needed to reproduce the simulations described here are made available via an openly available Zenodo dataset (`10.5281/zenodo.14368531`). All dynamic rupture simulations were performed using SeisSol (`www.seissol.org`), an open-source software freely available to download from `https://github.com/SeisSol/SeisSol/`. We use SeisSol, commit 60aedc8c (master branch on June 17, 2024). Instructions for downloading, installing, and running the code are available in the SeisSol documentation at `https://seissol.readthedocs.io/`. Downloading and compiling instructions are at `https://seissol.readthedocs.io/en/latest/compiling-seissol.html`. Instructions for setting up and running simulations are at `https://seissol.readthedocs.io/en/latest/configuration.html`. Quickstart containerized installations and introductory materials are provided in the docker container and jupyter notebooks at `https://github.com/SeisSol/Training`. Example problems and model configuration files are provided at `https://github.com/SeisSol/Examples`, many of which reproduce the SCEC 3D Dynamic Rupture benchmark problems described at `https://strike.scec.org/cvws/benchmark_descriptions.html`.

8 Declaration of Competing Interests

The authors declare no competing interests.

Acknowledgments

We thank the operators and hosts of the Ayiti-Séismes earthquake monitoring network at Bureau des Mines, Faculté des Sciences, Laboratoire URGéo, Université d'état d'Haïti, Ecole Normale Supérieur, and Laboratoire Géoazur for providing aftershock locations and making them free and openly available. We thank ESA for the rapid acquisition and distribution of Sentinel-1 data. We thank JAXA for access to ALOS-1 and ALOS-2 data.

This collaboration was supported by Geo-INQUIRE, a project funded by the European Commission under project number 101058518 within the HORIZON-INFRA-2021-

SERV-01 call (https://www.geo-inquire.eu/copyright/). Computing resources were provided by the Institute of Geophysics of LMU Munich **Oeser2006** and the Gauss Centre for Supercomputing (LRZ, project pn49ha) on the supercomputer SuperMUC-NG.

HZY acknowledges support by National Aeronautics and Space Administration (NASA), through the Future Investigators in NASA Earth and Space Science and Technology (FINESST) program (grant No. 80NSSC22K1533).

MM and AAG acknowledge additional support by Horizon Europe (grant No. 101093038, 101058129, and 101058518), NSF (grant No. EAR-2225286, EAR-2121568, OAC-2139536, OAC-2311208), and NASA (grant No. 80NSSC20K0495).

We gratefully acknowledge Jeremy Wong, Thomas Ulrich, and Jeena Yun for many helpful discussions related to SeisSol configurations and model setups. We also benefited greatly from discussions with Steeve Symithe and Eric Calais about the tectonic context, and conversations with Bryan Raimbault about the GNSS data and previous inversion results.

References

Aki, K., & Richards, P. G. (1980). *Quantitative seismology: Theory and methods*. W. H. Freeman.

Andrews, D. J. (1976). Rupture propagation with finite stress in antiplane strain. *Journal of Geophysical Research*, *81*(20), 3575–3582. https://doi.org/10.1029/JB081i020p03575

Aochi, H. (2003). The 1999 Izmit, Turkey, Earthquake: Nonplanar Fault Structure, Dynamic Rupture Process, and Strong Ground Motion. *Bulletin of the Seismological Society of America*, *93*(3), 1249–1266. https://doi.org/10.1785/0120020167

Aochi, H., & Ulrich, T. (2015). A Probable Earthquake Scenario near Istanbul Determined from Dynamic Simulations. *Bulletin of the Seismological Society of America*, *105*(3), 1468–1475. https://doi.org/10.1785/0120140283

Bakun, W. H., Flores, C. H., & Ten Brink, U. S. (2012). Significant Earthquakes on the Enriquillo Fault System, Hispaniola, 1500-2010: Implications for Seismic Hazard. *Bulletin of the Seismological Society of America*, *102*(1), 18–30. https://doi.org/10.1785/0120110077

Bizzarri, A., & Cocco, M. (2003). Slip-weakening behavior during the propagation of dynamic ruptures obeying rate- and state-dependent friction laws. *Journal of Geophysical Research: Solid Earth*, *108*(B8), 2002JB002198. https://doi.org/10.1029/2002JB002198

Calais, E., Freed, A., Mattioli, G., Amelung, F., Jónsson, S., Jansma, P., Hong, S.-H., Dixon, T., Prépetit, C., & Momplaisir, R. (2010). Transpressional rupture of an unmapped fault during the 2010 Haiti earthquake. *Nature Geoscience*, *3*(11), 794–799. https://doi.org/10.1038/ngeo992

Calais, E., Symithe, S., Monfret, T., Delouis, B., Lomax, A., Courboulex, F., Ampuero, J. P., Lara, P. E., Bletery, Q., Chèze, J., Peix, F., Deschamps, A., de Lépinay, B., Raimbault, B., Jolivet, R., Paul, S., St Fleur, S., Boisson, D., Fukushima, Y., … Meng, L. (2022). Citizen seismology helps decipher the 2021 Haiti earth-

quake. *Science*, *376*(6590), 283–287. https://doi.org/10.1126/science.abn1045

Calais, E., Symithe, S., Mercier de Lépinay, B., & Prépetit, C. (2015). Plate boundary segmentation in the northeastern Caribbean from geodetic measurements and Neogene geological observations. *Comptes Rendus. Géoscience*, *348*(1), 42–51. https://doi.org/10.1016/j.crte.2015.10.007

Calais, E., Symithe, S. J., & de Lépinay, B. M. (2023). Strain Partitioning within the Caribbean–North America Transform Plate Boundary in Southern Haiti, Tectonic and Hazard Implications. *Bulletin of the Seismological Society of America*, *113*(1), 131–142. https://doi.org/10.1785/0120220121

DeMets, C., Jansma, P. E., Mattioli, G. S., Dixon, T. H., Farina, F., Bilham, R., Calais, E., & Mann, P. (2000). GPS geodetic constraints on Caribbean-North America Plate Motion. *Geophysical Research Letters*, *27*(3), 437–440. https://doi.org/10.1029/1999GL005436

Douilly, R., Aochi, H., Calais, E., & Freed, A. M. (2015). Three-dimensional dynamic rupture simulations across interacting faults: The $\boldsymbol{M}_{\boldsymbol{w}}$ 7.0, 2010, Haiti earthquake. *Journal of Geophysical Research: Solid Earth*, *120*(2), 1108–1128. https://doi.org/10.1002/2014JB011595

Douilly, R., Haase, J. S., Ellsworth, W. L., Bouin, M.-P., Calais, E., Symithe, S. J., Armbruster, J. G., de Lepinay, B. M., Deschamps, A., Mildor, S.-L., Meremonte, M. E., & Hough, S. E. (2013). Crustal Structure and Fault Geometry of the 2010 Haiti Earthquake from Temporary Seismometer Deployments. *Bulletin of the Seismological Society of America*, *103*(4), 2305–2325. https://doi.org/10.1785/0120120303

Douilly, R., Mavroeidis, G. P., & Calais, E. (2017). Simulation of broad-band strong ground motion for a hypothetical Mw 7.1 earthquake on the Enriquillo Fault in Haiti. *Geophysical Journal International*, *211*(1), 400–417. https://doi.org/10.1093/gji/ggx312

Douilly, R., Paul, S., Monfret, T., Deschamps, A., Ambrois, D., Symithe, S. J., St Fleur, S., Courboulex, F., Calais, E., Boisson, D., de Lépinay, B. M., Font, Y., & Chèze, J. (2023). Rupture Segmentation of the 14 August 2021 Mw 7.2 Nippes, Haiti, Earthquake Using Aftershock Relocation from a Local Seismic Deployment. *Bulletin of the Seismological Society of America*, *113*(1), 58–72. https://doi.org/10.1785/0120220128

Dumbser, M., & Käser, M. (2006). An arbitrary high-order discontinuous Galerkin method for elastic waves on unstructured meshes - II. The three-dimensional isotropic case. *Geophysical Journal International*, *167*(1), 319–336. https://doi.org/10.1111/j.1365-246X.2006.03120.x

Farr, T. G., Rosen, P. A., Caro, E., Crippen, R., Duren, R., Hensley, S., Kobrick, M., Paller, M., Rodriguez, E., Roth, L., Seal, D., Shaffer, S., Shimada, J., Umland, J., Werner, M., Oskin, M., Burbank, D., & Alsdorf, D. (2007). The Shuttle Radar Topography Mission. *Reviews of Geophysics*, *45*(2), 2005RG000183. https://doi.org/10.1029/2005RG000183

Field, E. H., Arrowsmith, R. J., Biasi, G. P., Bird, P., Dawson, T. E., Felzer, K. R., Jackson, D. D., Johnson, K. M., Jordan, T. H., Madden, C., Michael, A. J., Milner,

K. R., Page, M. T., Parsons, T., Powers, P. M., Shaw, B. E., Thatcher, W. R., Weldon, R. J., & Zeng, Y. (2014). Uniform California Earthquake Rupture Forecast, Version 3 (UCERF3)–The Time-Independent Model. *Bulletin of the Seismological Society of America*, *104*(3), 1122–1180. https://doi.org/10.1785/0120130164

Gabriel, A.-A., Ulrich, T., Marchandon, M., Biemiller, J., & Rekoske, J. (2023). 3D Dynamic Rupture Modeling of the 6 February 2023, Kahramanmaraş, Turkey Mw 7.8 and 7.7 Earthquake Doublet Using Early Observations. *The Seismic Record*, *3*(4), 342–356. https://doi.org/10.1785/0320230028

Galis, M., Ampuero, J.-P., Mai, P. M., & Kristek, J. (2019). Initiation and arrest of earthquake ruptures due to elongated overstressed regions. *Geophysical Journal International*, *217*(3), 1783–1797. https://doi.org/10.1093/gji/ggz086

Garagash, D. I. (2021). Fracture mechanics of rate-and-state faults and fluid injection induced slip. *Philosophical Transactions of the Royal Society A: Mathematical, Physical and Engineering Sciences*, *379*(2196), 20200129. https://doi.org/10.1098/rsta.2020.0129

Glehman, J., Gabriel, A.-A., Ulrich, T., Ramos, M., Huang, Y., & Lindsey, E. (2024, August). Partial ruptures governed by the complex interplay between geodetic slip deficit, rigidity, and pore fluid pressure in 3D Cascadia dynamic rupture simulations. https://doi.org/10.31223/X5GH66

Goldberg, D. E., Koch, P., Melgar, D., Riquelme, S., & Yeck, W. L. (2022). Beyond the Teleseism: Introducing Regional Seismic and Geodetic Data into Routine USGS Finite-Fault Modeling. *Seismological Research Letters*, *93*(6), 3308–3323. https://doi.org/10.1785/0220220047

Harris, R. A., Barall, M., Andrews, D. J., Duan, B., Ma, S., Dunham, E. M., Gabriel, A.-A., Kaneko, Y., Kase, Y., Aagaard, B. T., Oglesby, D. D., Ampuero, J.-P., Hanks, T. C., & Abrahamson, N. (2011). Verifying a Computational Method for Predicting Extreme Ground Motion. *Seismological Research Letters*, *82*(5), 638–644. https://doi.org/10.1785/gssrl.82.5.638

Harris, R. A., Barall, M., Aagaard, B., Ma, S., Roten, D., Olsen, K., Duan, B., Liu, D., Luo, B., Bai, K., Ampuero, J.-P., Kaneko, Y., Gabriel, A.-A., Duru, K., Ulrich, T., Wollherr, S., Shi, Z., Dunham, E., Bydlon, S., ... Dalguer, L. (2018). A Suite of Exercises for Verifying Dynamic Earthquake Rupture Codes. *Seismological Research Letters*, *89*(3), 1146–1162. https://doi.org/10.1785/0220170222

Hayek, J. N., Marchandon, M., Li, D., Pousse-Beltran, L., Hollingsworth, J., Li, T., & Gabriel, A.-A. (2024). Non-Typical Supershear Rupture: Fault Heterogeneity and Segmentation Govern Unilateral Supershear and Cascading Multi-Fault Rupture in the 2021 Mw7.4 Maduo Earthquake. *Geophysical Research Letters*, *51*(20), e2024GL110128. https://doi.org/10.1029/2024GL110128

Heidbach, O., Rajabi, M., Cui, X., Fuchs, K., Müller, B., Reinecker, J., Reiter, K., Tingay, M., Wenzel, F., Xie, F., Ziegler, M. O., Zoback, M.-L., & Zoback, M. (2018). The World Stress Map database release 2016: Crustal stress pattern across scales. *Tectonophysics*, *744*, 484–498. https://doi.org/10.1016/j.tecto.2018.07.007

Heinecke, A., Breuer, A., Rettenberger, S., Bader, M., Gabriel, A.-A., Pelties, C., Bode, A., Barth, W., Liao, X.-K., Vaidyanathan, K., Smelyanskiy, M., & Dubey, P. (2014). Petascale High Order Dynamic Rupture Earthquake Simulations on Heterogeneous Supercomputers. *SC14: International Conference for High Performance Computing, Networking, Storage and Analysis*, 3–14. https://doi.org/10.1109/SC.2014.6

Hough, S. E., Martin, S. S., Symithe, S. J., & Briggs, R. (2023). Rupture Scenarios for the 3 June 1770 Haiti Earthquake. *Bulletin of the Seismological Society of America*, *113*(1), 157–185. https://doi.org/10.1785/0120220108

Ida, Y. (1972). Cohesive force across the tip of a longitudinal-shear crack and Griffith's specific surface energy. *Journal of Geophysical Research*, *77*(20), 3796–3805. https://doi.org/10.1029/JB077i020p03796

Jia, Z., Jin, Z., Marchandon, M., Ulrich, T., Gabriel, A.-A., Fan, W., Shearer, P., Zou, X., Rekoske, J., Bulut, F., Garagon, A., & Fialko, Y. (2023). The complex dynamics of the 2023 Kahramanmaraş, Turkey, M_w 7.8-7.7 earthquake doublet. *Science*, *381*(6661), 985–990. https://doi.org/10.1126/science.adi0685

Kaneko, Y., Lapusta, N., & Ampuero, J.-P. (2008). Spectral element modeling of spontaneous earthquake rupture on rate and state faults: Effect of velocity-strengthening friction at shallow depths. *Journal of Geophysical Research: Solid Earth*, *113*(B9), 2007JB005553. https://doi.org/10.1029/2007JB005553

Krenz, L., Uphoff, C., Ulrich, T., Gabriel, A.-A., Abrahams, L. S., Dunham, E. M., & Bader, M. (2021). 3D acoustic-elastic coupling with gravity: The dynamics of the 2018 Palu, Sulawesi earthquake and tsunami. *Proceedings of the International Conference for High Performance Computing, Networking, Storage and Analysis*, 1–14. https://doi.org/10.1145/3458817.3476173

Li, Z., & Wang, T. (2023). Coseismic and Early Postseismic Slip of the 2021 Mw 7.2 Nippes, Haiti, Earthquake: Transpressional Rupture of a Nonplanar Dipping Fault System. *Seismological Research Letters*, *94*(6), 2595–2608. https://doi.org/10.1785/0220230160

Ma, S., Custódio, S., Archuleta, R. J., & Liu, P. (2008). Dynamic modeling of the 2004 M_w 6.0 Parkfield, California, earthquake. *Journal of Geophysical Research: Solid Earth*, *113*(B2), 2007JB005216. https://doi.org/10.1029/2007JB005216

Madariaga, R. (1976). Dynamics of an expanding circular fault. *Bulletin of the Seismological Society of America*, *66*(3), 639–666. https://doi.org/10.1785/BSSA0660030639

Madden, E. H., Ulrich, T., & Gabriel, A.-A. (2022). The State of Pore Fluid Pressure and 3-D Megathrust Earthquake Dynamics. *Journal of Geophysical Research: Solid Earth*, *127*(4), e2021JB023382. https://doi.org/10.1029/2021JB023382

Martin, S. S., & Hough, S. E. (2022). The 8 April 1860 Jour de Pâques Earthquake Sequence in Southern Haiti. *Bulletin of the Seismological Society of America*, *112*(5), 2468–2486. https://doi.org/10.1785/0120220016

Maurer, J., Dutta, R., Vernon, A., & Vajedian, S. (2022, March). *Complex rupture and triggered aseismic creep during the August 14, 2021 Haiti earthquake from satel-*

lite geodesy (Preprint). Geodesy. https://doi.org/10.1002/essoar.10510731.1

Mercier de Lépinay, B., Deschamps, A., Klingelhoefer, F., Mazabraud, Y., Delouis, B., Clouard, V., Hello, Y., Crozon, J., Marcaillou, B., Graindorge, D., Vallée, M., Perrot, J., Bouin, M.-P., Saurel, J.-M., Charvis, P., & St-Louis, M. (2011). The 2010 Haiti earthquake: A complex fault pattern constrained by seismologic and tectonic observations: THE 2010 HAITI EARTHQUAKE FAULT PATTERN. *Geophysical Research Letters*, *38*(22), n/a–n/a. https://doi.org/10.1029/2011GL049799

Nielsen, S. B., Carlson, J. M., & Olsen, K. B. (2000). Influence of friction and fault geometry on earthquake rupture. *Journal of Geophysical Research: Solid Earth*, *105*(B3), 6069–6088. https://doi.org/10.1029/1999JB900350

Okuwaki, R., & Fan, W. (2022). Oblique Convergence Causes Both Thrust and Strike-Slip Ruptures During the 2021 M 7.2 Haiti Earthquake. *Geophysical Research Letters*, *49*(2), e2021GL096373. https://doi.org/10.1029/2021GL096373

Palgunadi, K. H., Gabriel, A.-A., Ulrich, T., López-Comino, J. Á., & Mai, P. M. (2020). Dynamic Fault Interaction during a Fluid-Injection-Induced Earthquake: The 2017 Mw 5.5 Pohang Event. *Bulletin of the Seismological Society of America*, *110*(5), 2328–2349. https://doi.org/10.1785/0120200106

Prentice, C. S., Mann, P., Crone, A. J., Gold, R. D., Hudnut, K. W., Briggs, R. W., Koehler, R. D., & Jean, P. (2010). Seismic hazard of the Enriquillo–Plantain Garden fault in Haiti inferred from palaeoseismology. *Nature Geoscience*, *3*(11), 789–793. https://doi.org/10.1038/ngeo991

Prentice, C. S., Mann, P., Peña, L. R., & Burr, G. (2003). Slip rate and earthquake recurrence along the central Septentrional fault, North American–Caribbean plate boundary, Dominican Republic. *Journal of Geophysical Research: Solid Earth*, *108*(B3), 2001JB000442. https://doi.org/10.1029/2001JB000442

Raimbault, B., Jolivet, R., Calais, E., Symithe, S., Fukushima, Y., & Dubernet, P. (2023). Rupture Geometry and Slip Distribution of the Mw 7.2 Nippes Earthquake, Haiti, From Space Geodetic Data. *Geochemistry, Geophysics, Geosystems*, *24*(4), e2022GC010752. https://doi.org/10.1029/2022GC010752

Raimbault, B. (2023, December). *Space-based seismotectonic of Hispaniola Island* [Doctoral dissertation, Université Paris sciences et lettres].

Ramos, M. D., Thakur, P., Huang, Y., Harris, R. A., & Ryan, K. J. (2022). Working with Dynamic Earthquake Rupture Models: A Practical Guide. *Seismological Research Letters*, *93*(4), 2096–2110. https://doi.org/10.1785/0220220022

Rice, J. R. (1992). Chapter 20 Fault Stress States, Pore Pressure Distributions, and the Weakness of the San Andreas Fault. In *International Geophysics* (pp. 475–503, Vol. 51). Elsevier. https://doi.org/10.1016/S0074-6142(08)62835-1

Saint Fleur, N., Dessable, J. E., Saint-Preux, G., Calais, É., Feuillet, N., Boisson, D., de Chabalier, J.-B., & Klinger, Y. (2024). Tectonic, Topographic, Geologic, and Hydroclimatic Influence on Crack Formation During the 2021 Haiti Earthquake. *Geochemistry, Geophysics, Geosystems*, *25*(7), e2023GC011255. https://doi.org/10.1029/2023GC011255

Saint Fleur, N., Feuillet, N., Grandin, R., Jacques, E., Weil-Accardo, J., & Klinger, Y. (2015). Seismotectonics of southern Haiti: A new faulting model for the 12 January 2010 *M* 7.0 earthquake. *Geophysical Research Letters*, *42*(23). https://doi.org/10.1002/2015GL065505

Saint Fleur, N., Klinger, Y., & Feuillet, N. (2020). Detailed map, displacement, paleoseismology, and segmentation of the Enriquillo-Plantain Garden Fault in Haiti. *Tectonophysics*, *778*, 228368. https://doi.org/10.1016/j.tecto.2020.228368

Simpson, R. W. (1997). Quantifying Anderson's fault types. *Journal of Geophysical Research: Solid Earth*, *102*(B8), 17909–17919. https://doi.org/10.1029/97JB01274

Symithe, S., Calais, E., de Chabalier, J. B., Robertson, R., & Higgins, M. (2015). Current block motions and strain accumulation on active faults in the Caribbean. *Journal of Geophysical Research: Solid Earth*, *120*(5), 3748–3774. https://doi.org/10.1002/2014JB011779

Symithe, S. J., Calais, E., Haase, J. S., Freed, A. M., & Douilly, R. (2013). Coseismic Slip Distribution of the 2010 M 7.0 Haiti Earthquake and Resulting Stress Changes on Regional Faults. *Bulletin of the Seismological Society of America*, *103*(4), 2326–2343. https://doi.org/10.1785/0120120306

Symithe, S., & Calais, E. (2016). Present-day shortening in Southern Haiti from GPS measurements and implications for seismic hazard. *Tectonophysics*, *679*, 117–124. https://doi.org/10.1016/j.tecto.2016.04.034

Taufiqurrahman, T., Gabriel, A.-A., Li, D., Ulrich, T., Li, B., Carena, S., Verdecchia, A., & Gallovič, F. (2023). Dynamics, interactions and delays of the 2019 Ridgecrest rupture sequence. *Nature*, *618*(7964), 308–315. https://doi.org/10.1038/s41586-023-05985-x

Tinti, E., Fukuyama, E., Piatanesi, A., & Cocco, M. (2005). A Kinematic Source-Time Function Compatible with Earthquake Dynamics. *Bulletin of the Seismological Society of America*, *95*(4), 1211–1223. https://doi.org/10.1785/0120040177

Tinti, E., Spudich, P., & Cocco, M. (2005). Earthquake fracture energy inferred from kinematic rupture models on extended faults. *Journal of Geophysical Research: Solid Earth*, *110*(B12), 2005JB003644. https://doi.org/10.1029/2005JB003644

Tinti, E., Casarotti, E., Ulrich, T., Taufiqurrahman, T., Li, D., & Gabriel, A.-A. (2021). Constraining families of dynamic models using geological, geodetic and strong ground motion data: The Mw 6.5, October 30th, 2016, Norcia earthquake, Italy. *Earth and Planetary Science Letters*, *576*, 117237. https://doi.org/10.1016/j.epsl.2021.117237

Ulrich, T., Gabriel, A.-A., Ampuero, J.-P., & Xu, W. (2019). Dynamic viability of the 2016 Mw 7.8 Kaikōura earthquake cascade on weak crustal faults. *Nature Communications*, *10*(1), 1213. https://doi.org/10.1038/s41467-019-09125-w

Uphoff, C., Rettenberger, S., Bader, M., Madden, E. H., Ulrich, T., Wollherr, S., & Gabriel, A.-A. (2017). Extreme scale multi-physics simulations of the tsunamigenic 2004 sumatra megathrust earthquake. *Proceedings of the International Conference for*

High Performance Computing, Networking, Storage and Analysis, 1–16. https://doi.org/10.1145/3126908.3126948

Wang, J., Mann, P., & Stewart, R. R. (2018). Late Holocene Structural Style and Seismicity of Highly Transpressional Faults in Southern Haiti. *Tectonics*, *37*(10), 3834–3852. https://doi.org/10.1029/2017TC004920

Wdowinski, S., & Hong, S.-H. (2012). Postseismic Deformation Following the 2010 Haiti Earthquake: Time-dependent Surface Subsidence Induced by Groundwater Flow in Response to a Sudden Uplift. *Fringe 2011 Workshop', Frascati, Italy, 19–23 September 2011.*

Wells, D. L., & Coppersmith, K. J. (1994). New empirical relationships among magnitude, rupture length, rupture width, rupture area, and surface displacement. *Bulletin of the Seismological Society of America*, *84*(4), 974–1002. https://doi.org/10.1785/BSSA0840040974

Wen, G., Li, X., Zhao, Y., Zhang, Y., Xu, C., & Zheng, Y. (2023). Kinematic Rupture Process and Its Implication of a Thrust and Strike-Slip Multi-Fault during the 2021 Haiti Earthquake. *Remote Sensing*, *15*(7), 1730. https://doi.org/10.3390/rs15071730

Wollherr, S., Gabriel, A.-A., & Mai, P. M. (2019). Landers 1992 "Reloaded": Integrative Dynamic Earthquake Rupture Modeling. *Journal of Geophysical Research: Solid Earth*, *124*(7), 6666–6702. https://doi.org/10.1029/2018JB016355

Yang, H., Yao, S., He, B., & Newman, A. V. (2019). Earthquake rupture dependence on hypocentral location along the Nicoya Peninsula subduction megathrust. *Earth and Planetary Science Letters*, *520*, 10–17. https://doi.org/10.1016/j.epsl.2019.05.030

Yin, H. Z., Xu, X., Haase, J. S., Douilly, R., Sandwell, D. T., & Mercier de Lepinay, B. (2022). Surface Deformation Surrounding the 2021 Mw 7.2 Haiti Earthquake Illuminated by InSAR Observations. *The Bulletin of the Seismological Society of America*, *113*, 41–57. https://doi.org/10.1785/0120220109
ADS Bibcode: 2023BuSSA.113...41Z.